Journal of Materials Chemistry B

ROYAL SOCIETY OF CHEMISTRY

REVIEW

View Article Online
View Journal | View Issue

Cite this: *J. Mater. Chem. B*, 2022, **10**, 7361

Emerging nanobiotechnology-encoded relaxation tuning establishes new MRI modes to localize, monitor and predict diseases

Taixia Wang,[ab] Xueni Zhang,[a] Yuan Xu,[a] Yingchun Xu,[a] Yifeng Zhang*[ab] and Kun Zhang*[ab]

Magnetic resonance imaging (MRI) is one of the most important techniques in the diagnosis of many diseases including cancers, where contrast agents (CAs) are usually necessary to improve its precision and sensitivity. Previous MRI CAs are confined to the signal-to-noise ratio (SNR) elevation of lesions for precisely localizing lesions. As nanobiotechnology advances, some new MRI CAs or nanobiotechnology-enabled MRI modes have been established to vary the longitudinal or transverse relaxation of CAs, which are harnessed to detect lesion targets, monitor disease evolution, predict or evaluate curative effect, *etc.* These distinct cases provide unexpected insights into the correlation of the design principles of these nanobiotechnologies and corresponding MRI CAs with their potential applications. In this review, first, we briefly present the principles, classifications and applications of conventional MRI CAs, and then elucidate the recent advances in relaxation tuning *via* the development of various nanobiotechnologies with emphasis on the design strategies of nanobiotechnology and the corresponding MRI CAs to target the tumor microenvironment (TME) and biological targets or activities in tumors or other diseases. In addition, we exemplified the advantages of these strategies in disease theranostics and explored their potential application fields. Finally, we analyzed the present limitations, potential solutions and future development direction of MRI after its combination with nanobiotechnology.

Received 21st March 2022,
Accepted 16th June 2022

DOI: 10.1039/d2tb00600f

rsc.li/materials-b

1. Introduction

Magnetic resonance imaging (MRI), due to its noninvasiveness and nonionizing radiation, is one of the most commonly utilized imaging techniques in both clinical and fundamental research.[1,2] In addition to the excellent penetration depth of MRI for tomography, it exhibits high spatial resolution in soft tissues, which has achieved significant progress in the

[a] *Central Laboratory and Ultrasound Research and Education Institute, Shanghai Tenth People's Hospital, Tongji University School of Medicine, No. 301 Yan-chang-zhong Road, Shanghai 200072, China. E-mail: zhangyifeng@tongji.edu.cn, zhang1986kun@126.com*

[b] *Shanghai Engineering Research Center of Ultrasound Diagnosis and Treatment, National Clinical Research Center for Interventional Medicine, Tongji University School of Medicine, No. 301 Yan-chang-zhong Road, Shanghai 200072, China*

Taixia Wang

Taixai Wang received her Bachelor's Degree at Tongji University. Currently, she is studying for her Master's Degree in Imaging Medicine and Nuclear Medicine at Tongji University. Her research interests include the synthesis of nanomaterials and functional nanomaterials for cancer diagnosis and treatment.

Xueni Zhang

Xueni Zhang is currently an undergraduate at Tongji University. Her research interests include the applications of nanomaterials in medicine and molecular medicine.

diagnosis, treatment monitoring and prognosis evaluation of many diseases, such as cancers.[3] It has been documented that many atom nuclei can be used in MRI, such as ^{1}H, ^{2}H, ^{11}B, ^{13}C, ^{19}F, ^{23}Na, ^{31}P, and ^{129}Xe,[4] among which ^{1}H-based MRI is the most prevalent imaging technique in clinical practice and biomedical research. The high sensitivity and abundance of ^{1}H lead to strong signals in ^{1}H MRI, thus offering precise anatomical and pathological information. However, ^{1}H also causes strong background signals, making ^{1}H MRI difficult to discern the nuance differences between the scarce critical cells and surrounding irrelevant cells.

In ^{1}H MRI, the relaxation process of hydrogen protons follows two distinct, independent and simultaneous pathways, *i.e.*, *T*1 and *T*2 relaxation.[5] To differentiate this nuance difference, contrast agents (CAs) are usually used to improve the precision and sensitivity of ^{1}H MRI, which shorten either the longitudinal (*T*1) or transverse (*T*2) relaxation times of water protons.[6] *T*1-weighted MRI CAs result in a positive/brighter contrast enhancement, while *T*2-weighted MRI CAs result in a negative/dark contrast enhancement.[7] The basic imaging principle of heteroatom MRI is approximately identical to that of ^{1}H MRI.[8] Among the nuclei, ^{19}F, which has relatively high sensitivity and extremely low biological signal background, is accepted to be an exceptional complement to ^{1}H in MRI;[9,10] however, its low sensitivity is still the major obstacle in the widespread application of ^{19}F MRI.

Empowered by the inspiring advancement of nanotechnology, recently some new nanobiotechnology-enabled MRI modes with specific applications have been established to vary the longitudinal or transverse relaxations of MRI CAs. Driven by the development of nanobiotechnology, novel concepts and advanced tools have been applied to overcome the shortcomings of conventional MRI CAs, and simultaneously establish new MRI modes to widen the application scope of MRI.[11] Besides exhibiting unique properties, these emerging nanobiotechnology-enabled MRI modes also exhibit unexpected capabilities including lesion target detection, lesion imaging localization, curative effect and prognosis evaluations and even imaging-guided treatment, which render the corresponding MRI CAs multi-functional nanoplatforms.[12] In the few past decades, a series of new design and synthesis strategies for MRI CAs based on MRI principles have been reported with in-depth and distinctive insights.[13] Nanoparticles for fabricating novel MRI CAs are burgeoning into an advanced field, and many reviews have been published. Among them, some focused on special nanomaterials such as superparamagnetic iron oxide nanoparticles (SPIONs)[14,15] and SPION-embedded polymeric nanoparticles[16] and discussed their biological applications including MRI CAs. Some reviews summarized the crucial preparation parameters and indispensable pre-treatment conditions of magnetic nanoparticles needed in MRI.[17] However, to the best of our knowledge, few reviews have focused on the advances in the design strategies of nanobiotechnology in smart relaxation tuning in response to the lesion microenvironment or specific targets, while their applications in the detection of biological targets or activity or monitoring in other diseases besides tumors have not been comprehensively discussed to date. Hence, in this review, we systematically summarize the design principles and potential applications of these new nanotechnology-originated MRI modes and the corresponding MRI CAs (Scheme 1), hopefully

Yuan Xu

Yuan Xu is currently an undergraduate student and about to attain his Bachelor's Degree from Tongji University in 2023. His research interest is focused on nano-biomedical materials.

Yingchun Xu

Yingchun Xu is currently an undergraduate and about to attain her Bachelor's Degree from Tongji University in 2022. Her research interests are focused on the association between nanometer materials science and medicine.

Kun Zhang

Kun Zhang, PhD, Professor, Deputy Director, Central Laboratory, Shanghai Tenth People's Hospital, Tongji University School of Medicine, National Science Fund for Outstanding Young Scholars, Shanghai Top-notch Youth Talent Support Program and Chair Professor for Bayu Scholar Program, His research fields include nanomedicine, ultrasound theranostics, immunotherapy, gene editing, tumor microenvironment modulation and monitoring, epigenetic modulation, regenerative medicine, and other interdisciplinarity research.

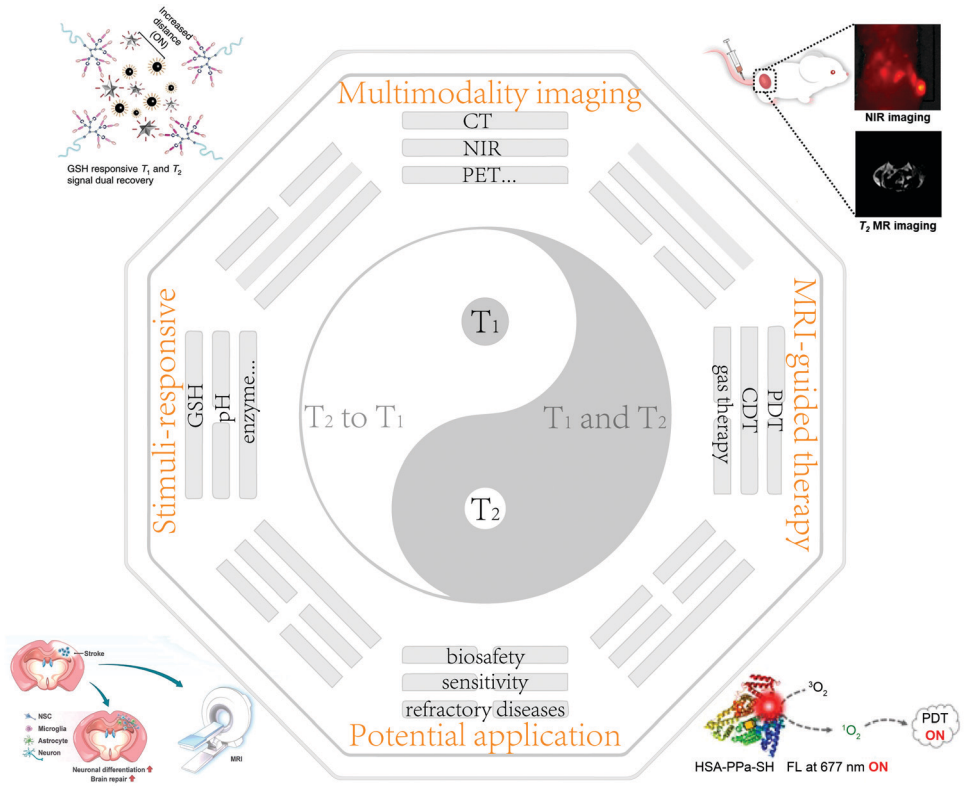

Scheme 1 Schematic of the design principles of nanobiotechnology and corresponding MRI CAs with their potential applications. Reproduced with permission from ref. 51. Copyright 2021, the American Chemical Society. Reproduced with permission from ref. 59. Copyright 2020, Wiley-VCH. Reproduced with permission from ref. 107. Copyright 2020, Springer Nature. Reproduced with permission from ref. 128. Copyright 2021, the American Chemical Society.

offering some guidance and distinctive insights into this field. Initially, the basic principles and classifications of current MRI and MRI CAs are outlined to give an initial impression, followed by the systematic elucidation of the cutting-edge progress in the design strategies of nanobiotechnologies and corresponding MRI CAs based on relaxation tuning. Subsequently, the advantages of these strategies over traditional MRI modes in biomedical and other potential applications will be exemplified with convincing and typical cases, among which their design principles are highlighted. Finally, the current challenges, potential solutions and future development direction of nanobiotechnology-enabled MRI modes and corresponding MRI CAs will be analyzed and deeply discussed.

2. Basic principles of MRI and common MRI CAs

Here, to understand MRI, its basic principles and common MRI CAs are introduced. MRI CAs were developed based on MRI, which can be used to enhance the contrast difference between the target and adjacent tissues.

2.1 Basic principles of MRI

The basic principles of MRI are shown in Fig. 1. In detail, as an external magnetic field (B_0) is applied, the magnetic spin moments of water protons tend to align with B_0, resulting in a net magnetization vector (M_0). When an orthogonal radiofrequency pulse is applied, the system can be energized and tends to "flip" the magnetic moments of proton nuclei towards the transversal plane. When the radiofrequency pulse is turned off, the magnetization returns to equilibrium through two distinct processes, *i.e.*, $T1$ and $T2$ relaxation.[5,18,19] $T1$ measures the recovery time of the initial longitudinal magnetic moments (M_0), while $T2$ measures the loss level of transverse magnetic moments due to dephasing.[20,21]

2.2 Conventional MRI CAs

Based on the principles of MRI, various MRI CAs have been developed and their electronic configuration has unpaired electrons, which means that they can change the local relaxation time of H nuclei. $T1$ MRI CAs can shorten the $T1$ relaxation time, finally leading to brighter images, which contain paramagnetic complexes or nanoparticles (NPs), *e.g.*, lanthanide ion gadolinium (Gd^{3+}) complexes and transition metal ion manganese (Mn^{2+})-based NPs.[22–25] $T2$ MRI CAs possess stronger ability to shorten the $T2$ relaxation, leading to a negatively enhanced MR signal and darker images. $T2$ MRI CAs specially refer to superparamagnetic iron oxide nanoparticles (SPIONs). MRI CAs are applied to shorten the relaxation rate ($r_{1,2} = 1/T1/2$) of protons in specific organs, tissues, and disease progression,

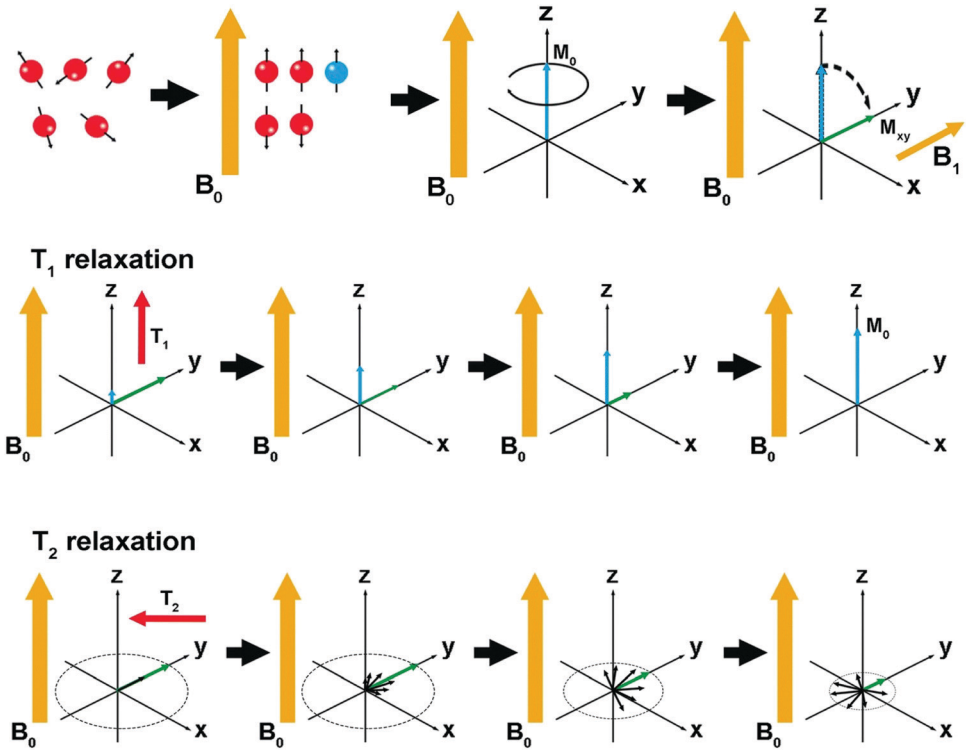

Fig. 1 Schematic representation of the basic principles of MRI. Reproduced with permission from ref. 19. Copyright 2019, Springer Nature.

thus positively or negatively enhancing their contrast and showing enhanced tumbling rates and increased relaxivity.[26,27]

2.2.1 Gd-based MRI CAs. Gd complex-based MRI CAs are used clinically, such as Gd-DTPA, which is frequently utilized as a *T*1 agent in clinics, featuring a short circulation time, low relaxivity and poor specificity.[28,29] Intriguingly, once these complexes are conjugated to nanoparticles, higher relaxivity can be achieved. As a paradigm, Yang *et al.*[30] utilized graphene quantum dots (GQD) as a support to carry Gd complexes and obtained paramagnetic GQDs (PGQD) after grafting polyethylene glycol (PEG) molecules. They found that regulating the molecular weight and molecular length of PEG could tune the longitudinal relaxivity of PGQD, and the largest relaxivity, which was 16-folder higher than that of Gd-DTPA. Li *et al.*[31] further demonstrated that the longitudinal magnetic relaxivities (r_1) of Gd^{3+} loaded on PEG-modified GQD could be effectively enhanced by modulating the localized superacid microenvironment to accelerate proton exchange. However, despite their widespread application in clinics, Gd deposits in living bodies will cause severe nephrogenic systemic fibrosis in patients whose renal function is imparied.[32] Furthermore, Gd deposits were detected in the brain tissues of patients without severe renal dysfuncction.[33]

2.2.2 Fe-based MRI CAs. Magnetic iron oxide nanoparticles (IONPs) are usually regarded as *T*2-weighted MRI CAs given that they can shorten the transverse relaxation time with satisfactory efficiency.[7] Great efforts and advances have been made to improve the *T*2-weighted MRI of IONPs by elevating their transverse magnetic relaxivities (r_2). In a recent study, Gu and coworkers[34] reported the preparation of layered double hydroxide (LDH)-stabilized IONPs with increased r_2 relaxivity, which could be attributed to the fact that the presence of hydroxyl groups in the LDH structure could augment the number of water molecules surrounding IONPs. It has been documented that the doping of fluoride ions (F^-) could also significantly elevate the r_2 value up to 526.5 by activating the synergistic contributions from the induced anisotropic morphology and particle aggregation of IONPs.[35]

Actually, Fe^{3+} ions have remarkable *T*1-weighted contrast enhancement effects. The unpaired spins of Fe^{3+} ions originate from their outer unpaired electrons. Based on this principle, Zhang and coworkers prepared a tumor microenvironment (TME)-activated nanoprobe for boosting the Fe-based *T*1 MRI by rearranging the d-electron spin direction of Fe^{3+} ions once they were released in the TME.[36] Also, surface modification could bind more water molecules adjacent to extremely small SPIONs *via* hydrogen bonding with coordinating phenoxide oxygens after binding with human serum albumin, which also resulted in an outstanding relaxation enhancement.[37]

Inspired by this, as the size of IONPs decreases, their magnetic moments will be reduced rapidly given that their surface area is enhanced and their volume magnetic anisotropy is reduced, which cooperatively suppress the *T*2 effect of IONPs, and simultaneously elevate their r_1 value,[38] eventually heightening the r_1/r_2 value, which is a key parameter in distinguishing *T*1 and *T*2 MRI CAs.[25] In this case, these IONPs, which are called extremely ultrasmall superparamagnetic iron oxide nanoparticles (USPIO NPs), have gained increasing interest.[39,40] Especially after appropriate modification (*e.g.*, Pepstatin A), USPIO NPs showed incomparable *T*1 MRI ability with r_1 = 4.16, which is close to that

of the clinical Gd-DTPA (4.43),[41] whose r_2/r_1 decreased to 5.35, indicating the high potential of *T*1-weighted MRI. Intriguingly, the stabilization of LDH could increase the space between ultrasmall Fe_3O_4 nanoparticles and reduce their magnetic coupling, which allowed the LDH-stabilized ultrasmall Fe_3O_4 to performance much better than free Fe_3O_4 in enhancing the *T*1 MRI effect.[42]

Biosafety is an important concern considering clinical translation, which determines that designing USPIO NPs with excellent biosafety is another direction or hotspot. Actually, due to their extremely small size (below 5 nm), USPIO NPs can cross the kidney filtration system, which allows their rapid excretion in the urine, guaranteeing their easy clearance and favorable biocompatibility in biological applications.[43] Xue *et al.*[44] developed nano-enabled, iron-based *T*1 MRI CAs without nephrotoxicity, which produced a significantly high signal-to-noise ratio (SNR) and rapid urine excretion, making them desirable for precisely localizing tumors *in vivo*. Thus, these *T*1-weighted MRI CAs are anticipated to be alternative clinical Gd-based CAs for patients with kidney dysfunction.

2.2.3 ^{19}F-based MRI CAs. ^{19}F imaging agents are another type of MR contrast agent that have been generally identified as ^{1}H relaxation agents. Different from ^{1}H agents, which highlight pathological features by exchanging the relaxation properties of the ^{1}H spins of the surrounding water molecules, the ^{19}F MR signal arises merely from the fluorine atoms contained in ^{19}F-based MRI CAs. The ^{19}F sources that can be utilized in ^{19}F MRI include perfluorocarbons (PFCs), trifluoromethyl compounds, fluorinated ionic liquids, and other fluorine-containing compounds. Excellent reviews focused on ^{19}F-based MRI CAs have been published. Some focused on their structure–property relationships and design parameters,[45] while others summarized the mechanisms and features of fluoropolymers in specific applications.[46] ^{19}F-based MRI CAs that can be activated upon interaction with special triggers are gaining increasing research interest. Zhang *et al.* fabricated a smart pH-activated ^{19}F MRI CA, which could be activated within the tumor microenvironment, detecting cancer with elevated precision and specificity.[47] The applications of ^{19}F MRI technology in various diseases will be further discussed in the following part of this review.

2.2.4 Multi-modal MRI CAs. It is well known that different imaging modalities have different merits or defects. To acquire comprehensive information on one lesion for precisely assessing the state of an illness, multi-modal imaging is indispensable, which can make up the shortcomings of each single imaging modality, such as *T*1 or *T*2 MRI, computed tomography (CT) imaging, fluorescence imaging (FLI), ultrasound contrast imaging (UCI), photoacoustic imaging (PAI), positron emission tomography (PET), and infrared thermal imaging (ITI).[48] The tremendous progress in nanotechnology, biomaterials, and materials science has offered more choices with more dual-, tri- and multi-modal molecular probes, arousing increasing interest and even driving the development of various multi-modal imaging apparatus.[49] In dual-modal probe design, Yong *et al.* combined MRI with CT to elevate the spatial resolution and realize real-time monitoring for precise tumor localization. Specifically, they synthesized an ultrasmall theranostic agent based on bovine serum albumin (BSA)-coated $GdW_{10}O_{36}$ nanoclusters (GdW_{10} NCs) for dual-modal bio-imaging.[50] Depending on the high r_1 relaxivity of Gd-containing polytungstates and the strong X-ray attenuation ability of Gd and W atoms, GdW_{10}@BSA NCs could be used as efficient dual-modal MRI/CT CAs (Fig. 2a). Chen and coworkers incorporated the high sensitivity of FLI in MRI and successfully developed an FLI/MRI dual-modal imaging nanoplatform consisting of a zinc-doped iron oxide core and fluorescent Cy5.5 tags.[51] The distribution of this nanoplatform in tumor was visualized *via* near-infrared (NIR)-FLI/MRI dual-modal imaging *in vivo*, hence enabling imaging-guided localization and safe treatment of tumors (Fig. 2b). Besides dual-modal molecular probes, tri- or multi-modal probes were also developed to combine more merits, provide functional and anatomical information and completely understand tumors, *e.g.*, MRI/UCI/CT,[48] MRI/PET/NIR,[52] and MRI/CT/PAI/ITI.[53]

Under the assistance of these molecular probes, imaging-guided therapy has been established to improve the treatment efficacy, precision and biosafety.[54] Typically, Zou *et al.* fabricated a dual-modal imaging theranostic system using hollow mesoporous Mn-doped silica shells modified with NIR-FLI molecules as carriers to load anti-tumor drugs.[55] The biodegradation of the Mn-doped shell in the acidic TME enabled TME-responsive dual-modal MR/NIR-persistent luminescence (PL) imaging, and concurrently efficiently promoted the controlled release of the loaded anti-tumor drugs for killing tumor cells without side effects.

3. MRI-guided cancer treatment

Imaging-guided treatment is also prevalent and attractive, which can elevate the biosafety and precision of disease treatment especially for interventional ablation and surgery, and meanwhile can effectively alleviate side effects and complications and repress tumor metastasis or reucrrence.[56] In the laboratory, the development of various MRI CAs has flourished in this field, laying a solid foundation for clinical translation.

3.1 MRI-guided photodynamic therapy

Photodynamic therapy (PDT) is a noninvasive therapeutic method, which employs photosensitizers (PSs) to convert oxygen into highly cytotoxic singlet oxygen ($^{1}O_2$) under light irradiation.[57,58] Although most photosensitizers can spontaneously emit fluorescence for FLI-guided PDT, these stimuli-responsive smart photosensitizers in imaging-guided PDT are also impeded by low-sensitivity and low spatial-resolution signals. Thus, to address this issue, An *et al.*[59] developed magnetic and fluorogenic nanoassemblies (NP-RGD) encapsulating PSs *via* the assembly of cRGD- and disulfide-containing paramagnetic small molecules (1RGD). As illustrated in Fig. 3a, NP-RGD exhibited a high MRI signal with quenched fluorescence and inhibited the PDT effect. Upon entering tumor cells *via* $\alpha v\beta 3$ integrin-mediated targeting delivery, the NP-RGD NPs were reduced by glutathione (GSH) and

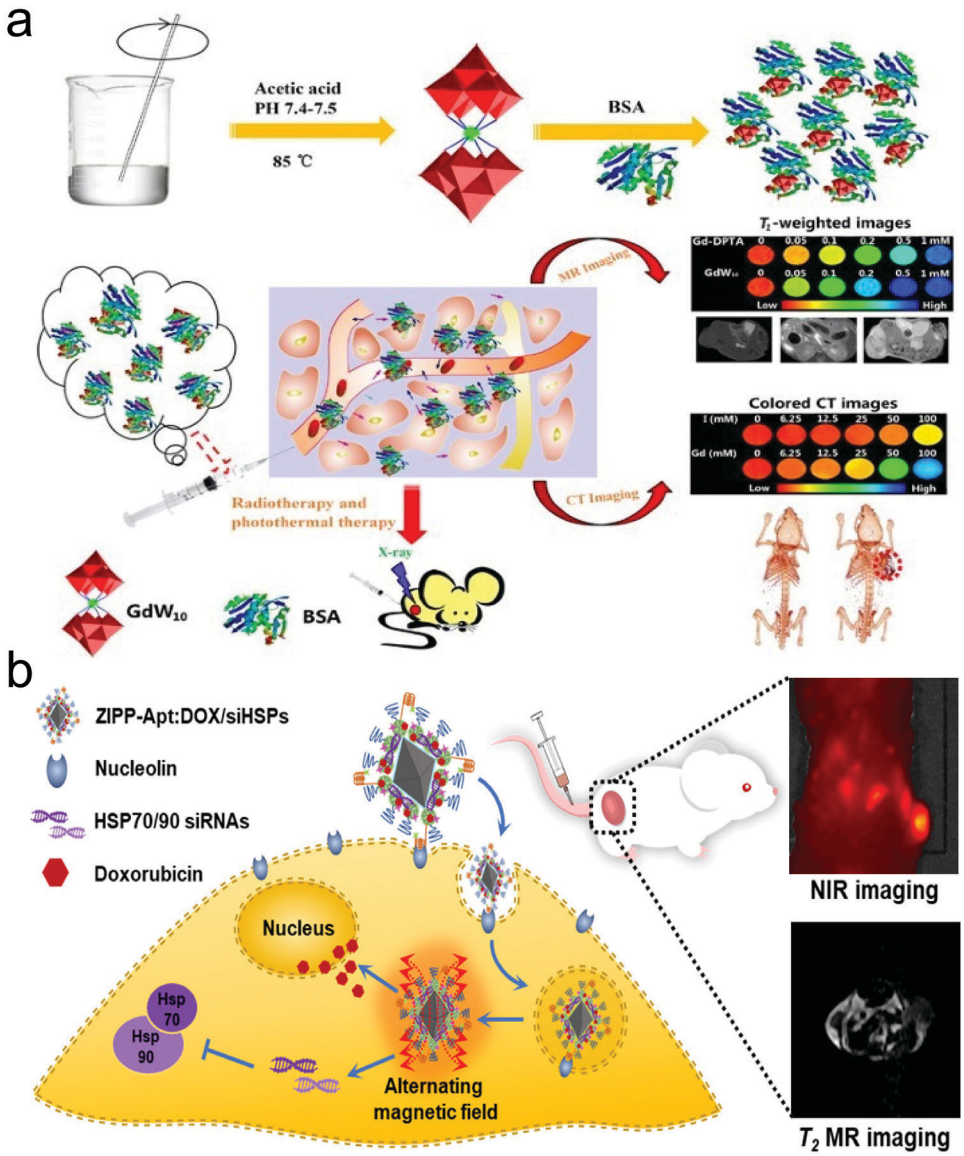

Fig. 2 (a) Schematic illustration of GdW_{10}@BSA NCs for dual-modal MR/CT imaging-guided photothermal therapy (PTT)/radiotherapy against cancer. Reproduced with permission from ref. 50. Copyright 2016, Springer Nature. (b) Schematic illustration of sensitized magneto-chemo theranostic agents. Reproduced with permission from ref. 51. Copyright 2021, the American Chemical Society.

disassembled into small-molecule probes (2RGD) and organic PSs (PPa-SH). PPa-SH could bind with intracellular albumin and trigger the cascade activation of fluorescence and PDT activity. NIR-FLI and MRI exhibited a synergistic effect to provide accurate bi-modal imaging information with the strongest FLI/MRI signal, highest SNR and considerably prolonged retention time to guide PDT (Fig. 3b and c), consequently resulting in the largest inhibitory rate (Fig. 3d). Tang's group reported the use of upconversion nanoparticles (UCNPs) and aggregation-induced emission (AIE)-active photosensitizers to fabricate a triple-jump photodynamic theranostic nanoplatform, exhibiting an unprecedented performance in FLI-MRI-guided PDT with high efficacy.[60]

The PDT efficacy is still hampered by the hypoxic tumor microenvironment and antioxidant-like GSH, which is another intractable concern.[61] Thus, great efforts have been devoted to improving the production of reactive oxygen species (ROS) under the guidance of MRI for precisely and highly efficiently improved PDT-based anti-tumor effects, *e.g.*, uniting chemotherapy and Fenton-like reactions enabled by Fe-based NPs to increase ROS production and alleviate hypoxia.[62] Also, catalase (CAT) and MnO_2 could be used to produce Mn^{2+} and deplete GSH to break the ROS and GSH-sustained redox balance, which are available for elevating the net content of PDT-provoked ROS and improving *T*1-weighted MRI.[63]

3.2 MRI-guided chemodynamic therapy

Chemodynamic therapy (CDT) is an emerging field, which has been systematically explored in cancer treatment. Different from PDT or sonodynamic therapy (SDT), which needs an external laser or ultrasound source to trigger ROS, the principle

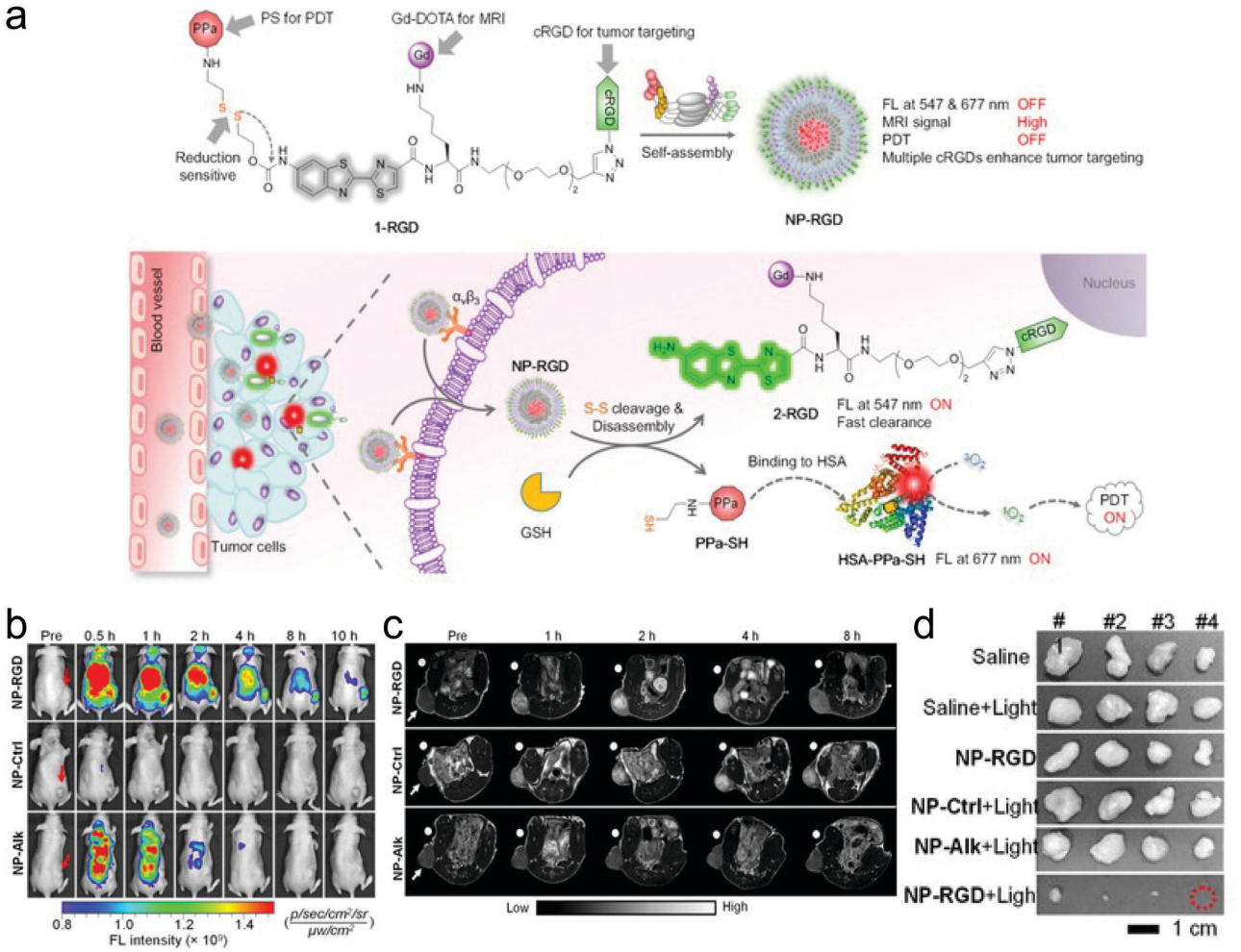

Fig. 3 (a) Schematic on how NP-RGD realized on-demand tumor PDT *via* cascade activation by intracellular GSH and albumin. (b) Fluorescence (FL) images and (c) FL intensities of U87MG tumor in mice receiving i.v. injection of NP-RGD, NP-Ctrl, or NP-Alk (200 μM, 200 μL) at 0 (Pre), 0.5, 1, 2, 4, 8, and 10 h. (d) Photographs of harvested U87MG tumors on day 16 after indicated treatments. Reproduced with permission from ref. 59. Copyright 2020 Wiley-VCH.

of CDT is to harness injected Fenton or Fenton-like agents to react with intratumoral H_2O_2 for the production of ROS and executing anti-tumor actions. Therefore, imaging guidance is more important for localizing, tracing and evaluating the retention of CDT agents in tumors, wherein MRI alone and MRI-containing multi-modal imaging have been used.[64] Typically, Wang *et al.* reported a novel *in situ* activatable CDT agent capable of inducing Fe^{2+} release to catalyze the oxidation of ascorbate monoanion ($AscH^-$) and produce H_2O_2 with improved efficacy, hence resulting in enhanced Fe-mediated *T*1-weighted MRI.[65]

3.3 MRI-guided hyperthermia therapy

Magnetic hyperthermia therapy (MHT) relies on the heat dissipation by magnetic nanoparticles upon exposure to an alternating magnetic field (AMF).[66] The contactless and localized heat production endow MHT with extraordinary advantages in the treatment of deep tumors.[67] MRI-guided MHT is easily accessible given that the existing magnetic IONPs, which are usually used as *T*2-weighted MRI CAs, can be harnessed to enhance MHT.[68–70] Shen *et al.*[71] functionalized $MnFe_2O_4$ NPs with Ir(III) complexes to construct Ir@$MnFe_2O_4$ nanoparticles to elevate the local temperature and induce mitochondrial damage and cell death upon exposure to AMF, during which Fe(III) was reduced to Fe(II) by the overexpressed GSH in the mitochondria of tumor cells, hence offering precise and effective treatment against cancer. Significantly, to address the failure of magnetic nanoparticles in providing real-time thermal feedback in MHT, Erving Ximendes and coworkers[72] integrated magnetic nanoparticles with infrared luminescent nanothermometers (LNTh; Ag_2S nanoparticles) in optomagnetic nanocapsules. In this strategy, the novel nanocapsules acted as multimodal CAs, providing accurate and real-time thermal feedback during *in vivo* controllable MHT and avoiding the collateral damage caused by overheating. Besides MHT, MRI-guided photothermal therapy (PTT) was also explored, *e.g.*, polydopamine shell-coated Fe_3O_4 (*i.e.*, Fe_3O_4@PDA) could lead to *T*2-weighted MRI-guided PTT against tumors.[73]

Our group used porous Fe_3O_4 as carriers to load DL-menthol and constructed a radiofrequency ablation (RFA)-enhancement agent (DLM@Fe_3O_4).[74] DL-Menthol (DLM)-induced inertial cavitation cooperated with Fe_3O_4-mediatd magnetothermal transformation to significantly enhance the RFA outcome against tumors given that cavitation has been widely accepted to elevate the transformation energy.[75–77] However, cavitation is uncontrollable, which probably results in injury to adjacent normal tissues. Fortunately, the loaded DLM made the surface of the Fe_3O_4 carriers hydrophobic and prevented H_2O from approaching to the paramagnetic Fe centers, receiving the quenched MRI. As DLM cavitation proceeded, the gradually decreased DLM in DLM@Fe_3O_4 increased the contact probability of Fe_3O_4 with H_2O and caused the gradual recovery of MRI. Therefore, the MRI signal variation could be used to monitor DLM cavitation and controllably and precisely ablate tumor without injures to adjacent normal tissues.

4. Nanobiotechnology-encoded relaxation tuning for localizing, monitoring and predicting diseases

Although the above-mentioned MRI CAs are empowered with robust *T*1 or *T*2 MRI with large r_1 or r_2 values, these conventional MRI CAs are local-concentration dependent and suffer from inherently low sensitivity given that an increase in dose cannot elevate the SNR, while facilely posing a high biosafety risk.[5] Inspiringly, great advances in constructing CAs to achieve higher relaxivity and/or enhanced accumulation in tissues of interest have been made to overcome these concerns. Especially, the stimulus-activated MRI CAs in response to various lesion microenvironments are favorable to significantly vary the relaxation time and establish new and distinctive MRI modes for directly improving the SNR and magnifying and localizing lesions.[78] Conversely, they can reflect and map the stimulated or activated microenvironment such as pH, hypoxia, specific species and targets (*e.g.*, lactate acid and enzymes). These biological targets or events (*e.g.*, pH, GSH, protease activity) have been quantitatively detected and even traced by FLI and PAI after designing rational molecular probes or nanoparticles,[79–81] which is a growing field deserving deep exploration. Here, we summarize the nanobiotechnology or MRI CAs-encoded relaxation tuning strategies after rational designs with emphasis on the created novel MRI modes and discuss their merits and properties in reflecting specific lesion microenvironments and localizing, monitoring, predicting and evaluating diseases.

4.1 Acidic microenvironment-induced generation of Mn^{2+} for tuning longitudinal relaxation

Mn-based NPs usually serve as *T*1 MRI CAs, but they are confronted with poor *T*1-weighted MRI ability due to their low r_1 value (<1). Instead, Mn^{2+} has a high magnetic moment and long electron spin relaxation time, which make Mn^{2+} ions ideal *T*1 MRI CAs with a much larger r_1 value (>5).[82] Especially after chelation and modification with ligands, the adsorbed water molecules on the outer sphere of Mn^{2+} complexes allowed molecule rotation to decrease and reinforce the *T*1 relaxivity of Mn^{2+} with a considerable increase in r_1 value.[83]

In particular, Mn-based NPs can respond to H^+ and release Mn^{2+} after the decomposition of NPs,[84,85] enabling intratumoral signal magnification with a high SNR, precision tumor localization, intratumoral pH detection to predict tumor progression and realizing prognosis evaluation.[84,86] It has been reported that Mn^{2+} can amplify the MR signals by interacting with proteins.[87,88] As a paradigm, Li and coworkers conjugated ultrasmall manganese ferrite nanoparticles (UMFNPs) with a class of pentapeptide Cys-Arg-Glu-Lys-Ala (CREKA) to synthesize an ultrasensitive *T*1-weighted MRI probe (UMFNP-CREKA) (Fig. 4a).[89] In response to the unique pathological environments of metastases (low pH = 6.5 and rich H_2O_2), Mn^{2+} ions were released from the nanoprobe, successfully contributing to the increase in r_1 value, especially after binding with 10% fetal bovine serum (FBS) (Fig. 4b). This acidic TME-activated Mn^{2+} release successfully elevated the SNR of *T*1-weighted MRI images, as shown in 3D *T*1 MRI (Fig. 4c), wherein the whole tumor was illuminated after administrating UMFNP-CREKA, whereas the surrounding normal tissues had no significant contrast enhancement.

Also, Mi and coworkers designed Mn^{2+}-doped calcium phosphate (CaP) nanoparticles,[90] followed by PEG modification (Fig. 4d). These MnCaP-PEG nanoparticles were accessible to subject them to H^+ erosion for releasing Mn^{2+}, which could be used to tune the longitudinal relaxation and achieve a larger r_2 value after chelating with proteins (Fig. 4e). Based on this, these types of nanoparticles can be designed to respond to the acidic TME and specifically magnify the *T*1-weighted MRI signal of tumors for localizing undetectable metastatic tumors and indirectly reflecting the pH distribution after intravenous injection (Fig. 4f). Considering the fact that the tumor acidity positively correlates with the lactate acid level, which is manipulated by anaerobic metabolism (hypoxia), these nanoparticles can also indirectly map the distributions of hypoxia (Fig. 4g and h) and lactate acid (Fig. 4i and j).

4.2 MRI CA aggregation or disintegration-enabled relaxation tuning for brightening tumor and detecting targets

MRI CAs have aroused considerable interest given that they can serve as magnetic signal transducers for magnetic sensing.[91,92] However, due to the dependence on the state change of magnetic nanoparticles, traditional *T*2-based magnetic immunosensors exert signals that are not sensitive enough to detect the trace amounts of targets, and meanwhile could be interfered by nonspecific aggregation easily.[93] It has been accepted that the MRI property is dependent on the structure and surface state of MRI CAs, based on which the aggregation or disintegration of MRI CAs is envisioned to switch 'on' or 'off' the *T*1 or *T*2 MRI signals or vary their longitudinal and transverse relaxations (r_1/r_2) in response to biological targets or events including acidity, GSH, hypoxia, specific species and targets (*e.g.*, lactate acid and protease) in the disease microenvironment.[94] The alteration in on/off or off/on switching in *T*1 or/and *T*2 MRI signals can reflect or even track these biological targets or events.

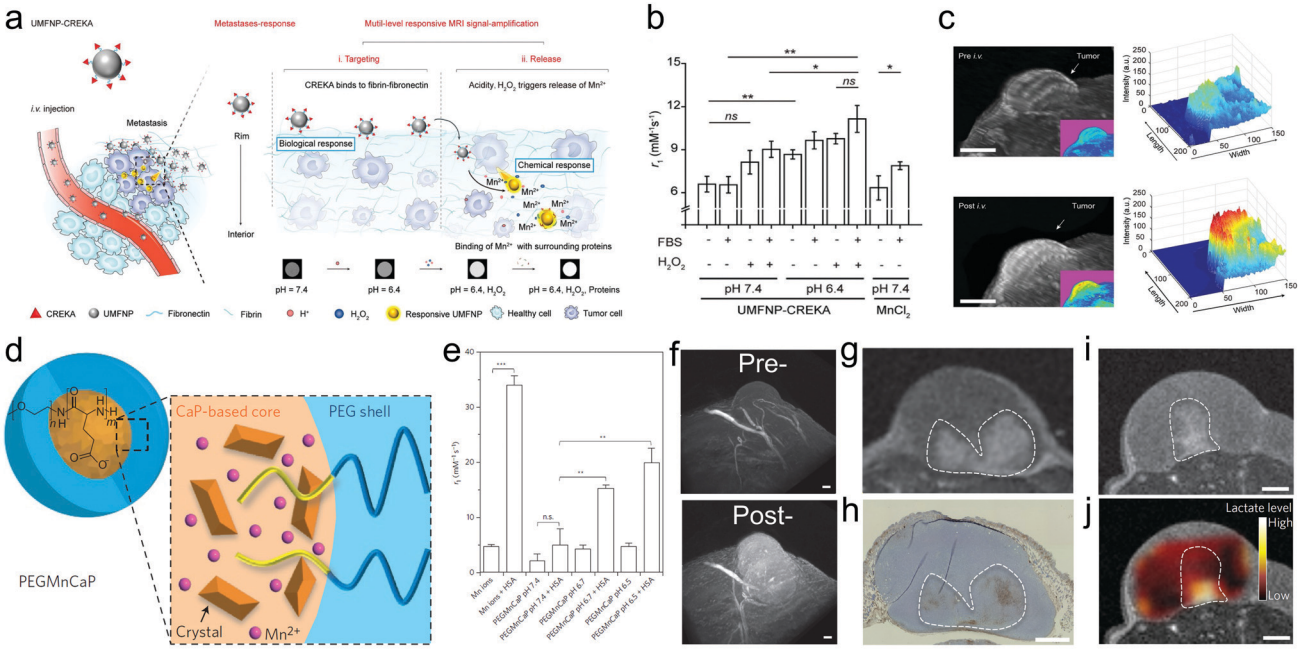

Fig. 4 (a) Schematic illustration of the bioinspired UMFNP-CREKA nanoprobe with multilevel responsive *T*1-weighted MR signal-amplification capabilities for illuminating ultrasmall metastases. (b) r_1 values from *T*1-weighted MR images of UMFNP-CREKA incubated in the indicated conditions for 12 h. (c) 3D MR images of the subcutaneous breast tumor before and at 50 min after intravenous injection of UMFNP-CREKA. Reproduced with permission from ref. 89. Copyright 2019, Wiley-VCH. (d) Structural depiction of the PEG-modified and Mn-doped CaP NPs (PEGMnCa). (e) r_1 value of PEG-MnCaP NPs in human serum albumin (HSA)-free or HSA-contained dispersion with varying pH values. (f) 3D MRI images of C26 tumors at pre- and 1 h later post-injection of PEG-modified MnCaP NPs under the 7 T magnetic field, scale bar: 50 μm. MRI image (g) and optical hypoxia-stained image (h) of C26 tumor 4 h after 4 h post-injection of PEG-modified MnCaP NPs under a 1 T magnetic field, scale bar: 1 mm. MRI image (i) and chemical-shift image (j) of C26 tumors after injecting PEG-modified MnCaP and (g) under 7 T magnetic field, scale bar: 1 mm. Reproduced with permission from ref. 90. Copyright 2016, Springer Nature.

Long and coworkers synthesized two sets of IONPs,[95] which allowed the transformation of monodispersed sate to aggregate to enhance the *T*2 signal upon sensing matrix metalloproteinase (MMP) enzymes (Fig. 5a). Once they entered cells that expressed MMP2/9 and CXCR4, the nanoengineered novel IONPs would be activated into a self-assembled superparamagnetic nanocluster network. Consequently, a *T*2 signal enhancement with around 160% enhancement from the 'off' state to 'on' state was acquired, providing an opportunity to detect MMP activity at the cellular level (Fig. 5b). Notably, the disaggregation transformation into self-aggregation for altering the relaxation or switching on the MRI signal can be also activated by H^+, which indicates the feasibility of H^+ detection using this strategy.[96]

Although the above-mentioned transformation of the monodispersed state to aggregation can enhance MRI, most cases highlight the aggregation transformation to disintegration activated by some specific tumor targets for realizing the switching of MRI signals from 'on' to 'off' or from *T*1 to *T*2, and *vice versa*. Typically, Yi constructed $NaGdF_4$&$CaCO_3$ co-loaded nanospheres coated with polymeric shells and cell membrane in sequence (Fig. 5c), wherein the polymeric shells served as blocking layers to prevent H^+ erosion and sustain the 'off' *T*1 MRI signal of Gd^{3+} in $NaGdF_4$ by the confinement-blockaded interaction between H_2O and Gd^{3+} (Fig. 5d).[97] As the nanospheres were engulfed by cells, the H^+ in the acidic microenvironment could erode and decompose the $CaCO_3$ NPs into CO_2 bubbles and destroy the nanospheres, consequently making the $NaGdF_4$ nanoparticles exposed and changing the aggregation state into a disintegrated state (Fig. 5d). This promoted the interaction of Gd^{3+} in $NaGdF_4$ and H_2O and led to *T*1 MRI signal recovery ('on' state) (Fig. 5e). This work not only magnified and localized the tumor with a considerably elevated SNR (Fig. 5f), but also traced or detected the acidity or pH value in the tumor.

Intriguingly, the *T*1/*T*2 signal exchange by varying their aggregation or disaggregation state to simultaneously tune their transverse and longitudinal relaxations is also available for detecting specific tumor targets. As a paradigm, Ma *et al.* reported the preparation of USPIO NP-assembled nanoclusters, and cystamine dihydrochloride (Cys) was used to connect these USPIO NPs, endowing the nanoclusters with robust *T*2-weighted MRI property (Fig. 5g).[98] Under the reducing agent (*e.g.*, GSH) in tumor cells, the disulfide bonds in Cys could be broken, and the USPIO NP-assembled nanoclusters disintegrated and became monodispersed. At this time, the *T*2-weighted MRI was impaired and the *T*1-weighted MRI recovered, resulting in 'off' *T*2 and 'on' *T*1 MRI (Fig. 5g), which was available for detecting the GSH level.

4.3 Aggregated MRI CA disintegration for monitoring drug release

Actually, aggregation transformation into the monodispersed sate also favors drug release monitoring, which is beneficial for

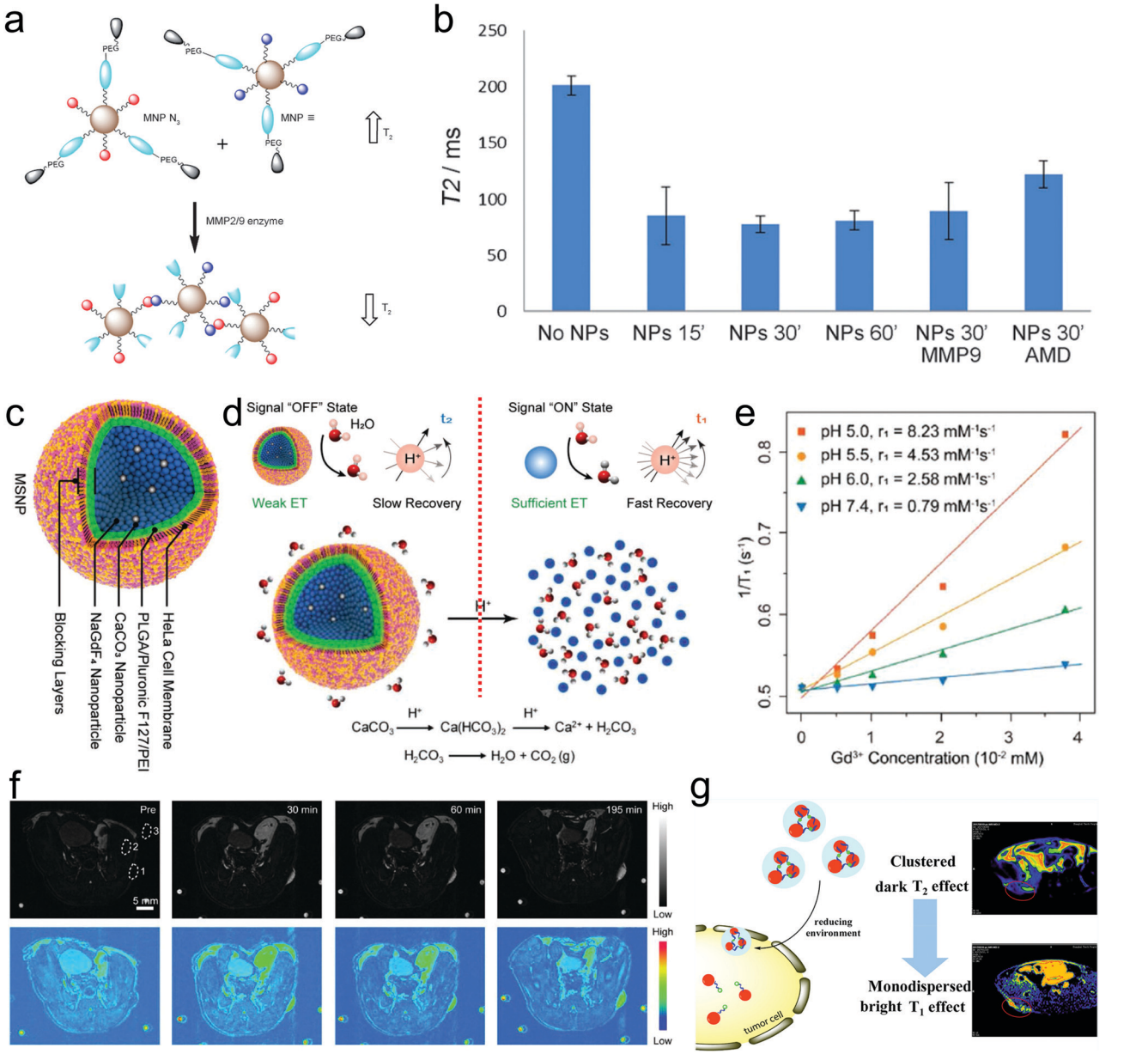

Fig. 5 (a) Schematic illustration of MMP-activated particle aggregation. (b) Transverse (*T*2) relaxation time of U87 cells highly expressing CD4 and CXCR4 and embedded in 1% agarose gel containing Fe_3O_4 nanoparticles with or without exogenous MMP9 or the CXCR4 blockading agent AMD3100. Reproduced with permission from ref. 95. Copyright 2014, Wiley-VCH. (c) Structural depiction of $NaGdF_4$&$CaCO_3$ co-loaded nanospheres coated with polymeric shells and cell membrane in sequence. (d) Schematic illustration explaining the principles of 'off' and 'on' states of *T*1-weighted MRI signals in response to H^+. (e) Gd^{3+} concentration-dependent longitudinal relaxivity profiles at different pH values for calculating the r_1 values and (f) *T*1 MRI images and pseudo-color images of one tumor-implanted mouse before (pre-) and after different time points post-administering of these probes. Reproduced with permission from ref. 97. Copyright 2019 Wiley-VCH. (g) Schematic illustration of the switching of USPIO NP-assembled nanoclusters to monodispersed sate in response to reducing agent for brightening tumor *via* switching *T*2 and *T*1 MRI signals. Reproduced with permission from ref. 98. Copyright 2019, the American Chemical Society.

evaluating and predicting treatment outcomes. Enlightened by the IONP aggregate disintegration-enhanced MRI, anti-tumor drugs can be co-loaded with particle aggregates in pH-sensitive carriers. Upon entry in the acidic TME, the carriers are degraded to release IONPs and anti-tumor drugs, and the switch of the IONPs state from aggregation to disintegration can enhance the MRI signal for reflecting anti-tumor drug release.[99] Typically, Zhao *et al.* loaded manganese arsenite complexes that served as the prodrug of arsenic trioxide (ATO) in hollow silica vehicles, wherein the loaded manganese arsenite complexes could respond to the acidic microenvironment and generate Mn^{2+} after their decomposition and release ATO. Mn^{2+} can enhance *T*1-weighted MRI, enabling the real-time monitoring of the ATO release.[100] Besides shaping into pro-drugs *via* chelation with anti-tumor drugs, Mn-based NPs could be directly utilized with anti-tumor drugs on MSN, and

Mn^{2+} release in response to acid, oxidative stress and redox elevated *T*1 MRI visualization to monitor anti-tumor drug release.[101]

4.4 Distance-dependent relaxation tuning for detecting targets

Traditional MRI CAs are usually effective in either the *T*1 or *T*2 imaging mode. However, the drawbacks such as the short circulation time of *T*1 MRI CAs and the susceptibility artifacts of *T*2 MRI CAs are always inevitable.[102,103] The challenges in combining the strong *T*1 and *T*2 contrast effects in a single CA are mostly ascribed to the strong magnetic coupling between the CAs of *T*1 and *T*2.[104] Thus strategies to overcome these setbacks have been put proposed. Herein, a distance-dependent magnetic resonance tuning (MRET) strategy was established and the corresponding MRI CAs comprising a paramagnetic *T*1 MRI 'enhancer' (*e.g.*, Gd-DOTA) and a superparamagnetic *T*2 MRI 'quencher' (*e.g.*, $Zn_{0.4}Fe_{2.6}O_4$) were developed.[105] The MRET principle was based on the fact that the Gd-DOTA-mediated *T*1 MRI signal was 'off' as the separation distance between $Zn_{0.4}Fe_{2.6}O_4$ and Gd-DOTA was close due to the slow water proton spin relaxation and the slow electron spin fluctuation in $Zn_{0.4}Fe_{2.6}O_4$. In contrast, as they were separated from each other, the water proton spin relaxation and electron spin fluctuation in $Zn_{0.4}Fe_{2.6}O_4$ were concurrently accelerated, leading to 'on' *T*1-weighted MRI (Fig. 6a and b). According to the cleavage or binding with different molecules on the enhancer and quenchers, respectively, this MRET strategy could serve as an MRI-based sensor for detecting both molecular interactions (*e.g.*, binding, cleavage, and reversible protein folding/unfolding) and biological targets (*e.g.*, H_2O_2, MMP2, Cu^+, DNA, H^+, Hg^+ and ethylene diamine tetraacetic acid (EDTA)) (Fig. 6c). Besides biological activities and disease targets, MRET could be used to detect biological electricity. Typically, Wang *et al.* reported the preparation of injectable USPIO NP-aggregated clusters (enhancer) entrapped in paramagnetic polymers (quencher), wherein the *T*1 MRI signal of the clusters was quenched by polymers.[106] Once they entered the epilepsy zone, the abnormal electric discharging during epilepsy seizure could widen the distance between the polymer and clusters, restoring the *T*1 MRI signal and realizing epilepsy visualization with high sensitivity and SNR (Fig. 6d).

Actually, based on the magnetism-based nanoscale MRET, dynamical "*T*2 and *T*1" dually-switchable MRI CAs could be developed to simultaneously activate *T*1 and *T*2 MRI signals for

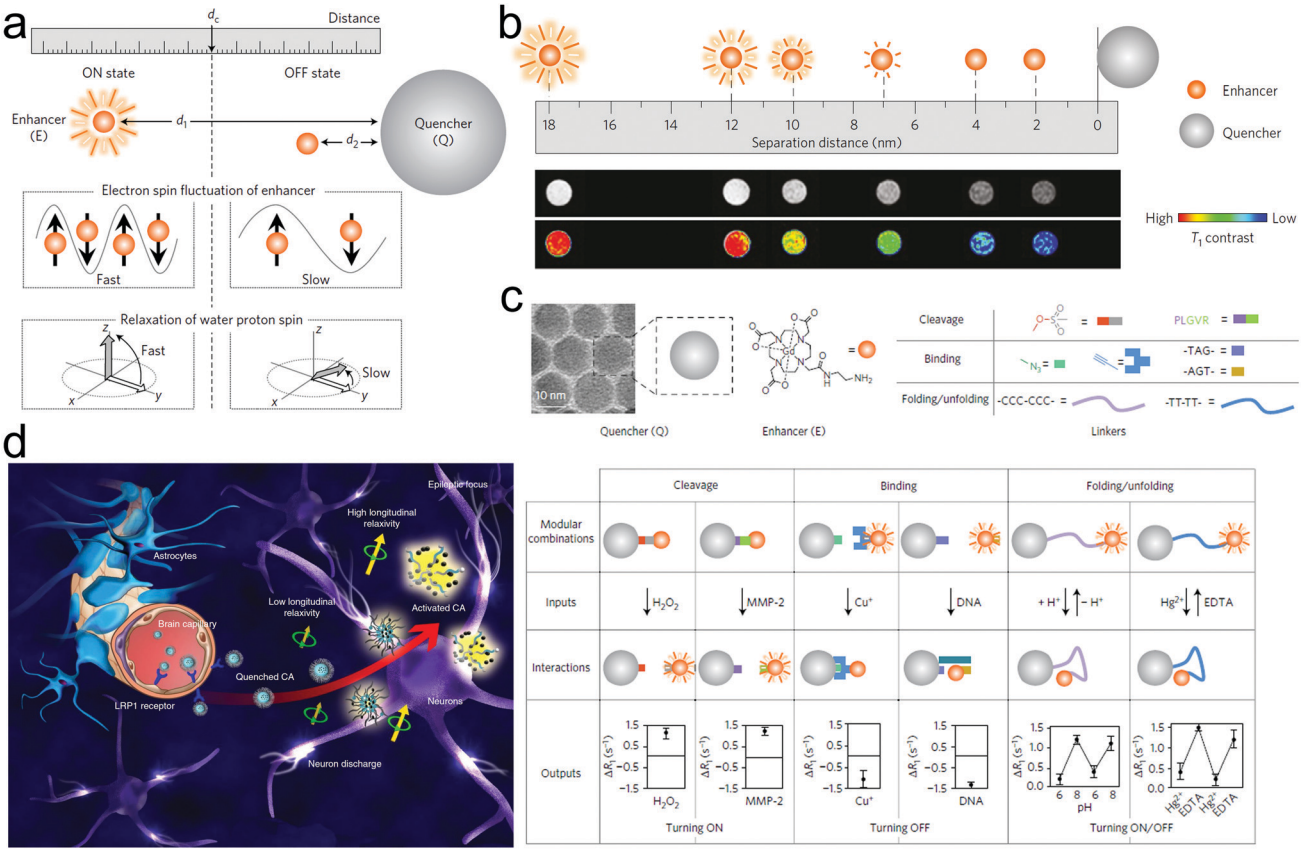

Fig. 6 (a) Schematic of MRET principle for illustrating how the distance variation between the enhancer and quencher influences the electron spin and proton spin relaxation. (b) Distance expanding schematic (upper) and corresponding MRI images (bottom) of these enhancer–quencher conjugates in response to their distance variation. (c) Types of quenchers, enhancers, inputs, interactions and outputs in distance-dependent MRET-based probes for distinguishing biological interactions including cleavage, binding and folding/unfolding and detecting various targets. Reproduced with permission from ref. 105. Copyright 2019, Springer Nature. (d) Schematic illustration of electrical field-activated MRET for monitoring abnormal electricity in epilepsy seizure and illuminating the epilepsy zone using *T*1-MRI. Reproduced with permission from ref. 106. Copyright 2021, Springer Nature.

detection.[43] Wang *et al.* introduced new two-way MERT (TMRET) nanotechnology with dually-activatable *T*1 and *T*2 signals.[107] TMRET nanotechnology was constructed *via* the co-encapsulation of paramagnetic Mn^{2+} (P–Mn) chelates and SPIONs in a disulfide-crosslinked micelle (Fig. 7a). Both the *T*1 and *T*2 MRI signals were turned 'off' when the TMRET pair was 'locked' closely in the micelle core. After interacting with biological stimuli (*e.g.*, GSH) to modulate the integrity of the micelles (Fig. 7b), both the *T*1 and *T*2 MRI signals were turned 'on' as the distance between Mn^{2+} and SPION increased, enabling the detection of GSH *in vitro* and *in vivo*. Pan and coworkers proposed an *in situ* stimuli-triggered *T*1–*T*2 switchable MRI nanoprobe, with IONPs modified with HA,[108] and the underlining mechanism is illustrated in Fig. 7c. Before modification with hyaluronic acid (HA), the monodispersed IONPs chelated with polyacrylic acid showed a strong *T*1 contrast enhancement effect with r_1 = 2.227 mM^{-1} s^{-1} and r_2/r_1 ratio = 3.211 (Fig. 7d). After stimulation in an acid environment, the HA-modified IONP-polyacrylic acid nanoparticles (IONP-HP) underwent self-assembly to form nanoclusters, leading to a *T*2 MRI enhancement (Fig. 7e).

4.5 TME-activatable relaxation tuning for monitoring targets and biological events

Although the MRET and its derived TMRET strategies mentioned above offer unique approaches to improve the sensitivity in tumor imaging,[105,107] the special structure consisting of an enhancer and quencher whose selection and connection need precise and rational design to desired targets or biological process, limits its application domain. Herein, various microenvironment-activatable magnetic resonance relaxation tuning strategies have been developed with the facile synthesis and design of the corresponding MRI CAs, showing widespread application potential.

Firstly, a new MRI technique, *i.e.*, chemical exchange saturation transfer (CEST), was established to indirectly detect non-labelled and native molecules, wherein the water proton signal through selective saturation of exchangeable protons could be manipulated.[109] Based on a furin-mediated 2-cyanobenzothiazole

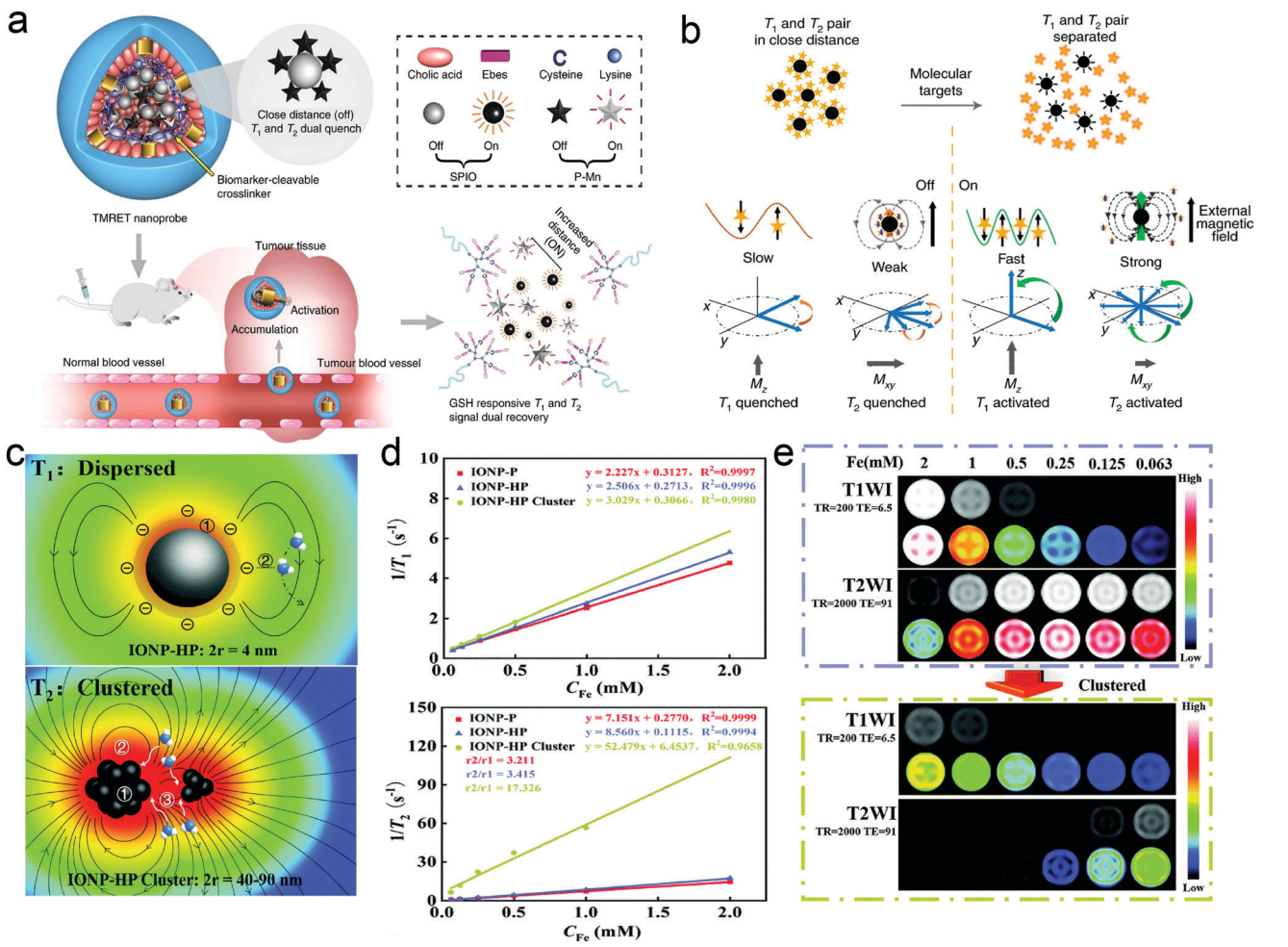

Fig. 7 (a) Schematic illustration of TMRET nanotechnology. (b) Illustration of the mechanism of *T*1 and *T*2 quenching and recovery in the TMRET nanoprobe. Reproduced with permission from ref. 107. Copyright 2020, Springer Nature. (c) Schematic illustration of the correlation between *T*1/*T*2 relaxation and the associated parameters. (d) *T*1 and *T*2 relaxation rates of IONP-P, IONP-HP, and IONP-HP clusters at a magnetic field of 1.5 T. (e) *T*1- and *T*2-weighted images of IONP-HP before and after clustering at different Fe concentrations on a 1.5 T MRI scanner. Reproduced with permission from ref. 108. Copyright 2021, The Royal Society of Chemistry.

(CBT)-Cys click reaction, Yuan *et al.* constructed an intracellular conjugate molecule consisting of the anticancer agent Olsalazine (Olsa) and cell-penetrating peptide RVRR (Olsa-PVRR).[110] As Olsa-PVRR molecules entered tumor cells, they further self-assembled into Olsa-PVRR NPs under the activation of tumor-associated enzyme furin, consequently varying the CEST MRI signals for assessing tumor aggressiveness and predicting therapeutic outcomes (Fig. 8a). Interestingly, this modality could be reinforced and enriched after incorporating imaging/diagnosis units (*e.g.*, Gd^{3+} doping).[111]

A redox-activatable relaxation tuning strategy for the detection of GSH was also established and various imaging designs and corresponding CAs were designed. Typically, Mn-based nanoparticles with a high valence (*e.g.*, +4) can be reduced to Mn^{2+} by intratumoral GSH, which can also specifically brighten tumors and reversibly reflect the GSH level.[112] Zhang *et al.* also reported an Fe_3O_4 nanoparticle-based GSH-responsive MRI probe with simple structure and small dimensions,[113] which exhibited interlocked responses of $T1$ and $T2$ signals upon reaction with GSH. Moreover, according to their theoretical analysis, they established a mathematic model and realized quantitative mapping of the GSH distribution in brain gliomas through MRI (Fig. 8b). In another study, it was reported that the marriage of concurrent widefield optical imaging and functional MRI could simultaneously realize the fluorescent measurement of the whole brain blood oxygen level and whole-cortex calcium ions for monitoring brain activity, which is beneficial for a comprehensive understanding of brain function.[114]

Reactive oxygen species or reactive nitrogen species that sustain the redox balance with reducing species have been demonstrated to be correlated with many biological processes, *e.g.*, vascular homeostasis, cancer evolution, stem cell differentiation, bacterial infection, and inflammation.[115–118]

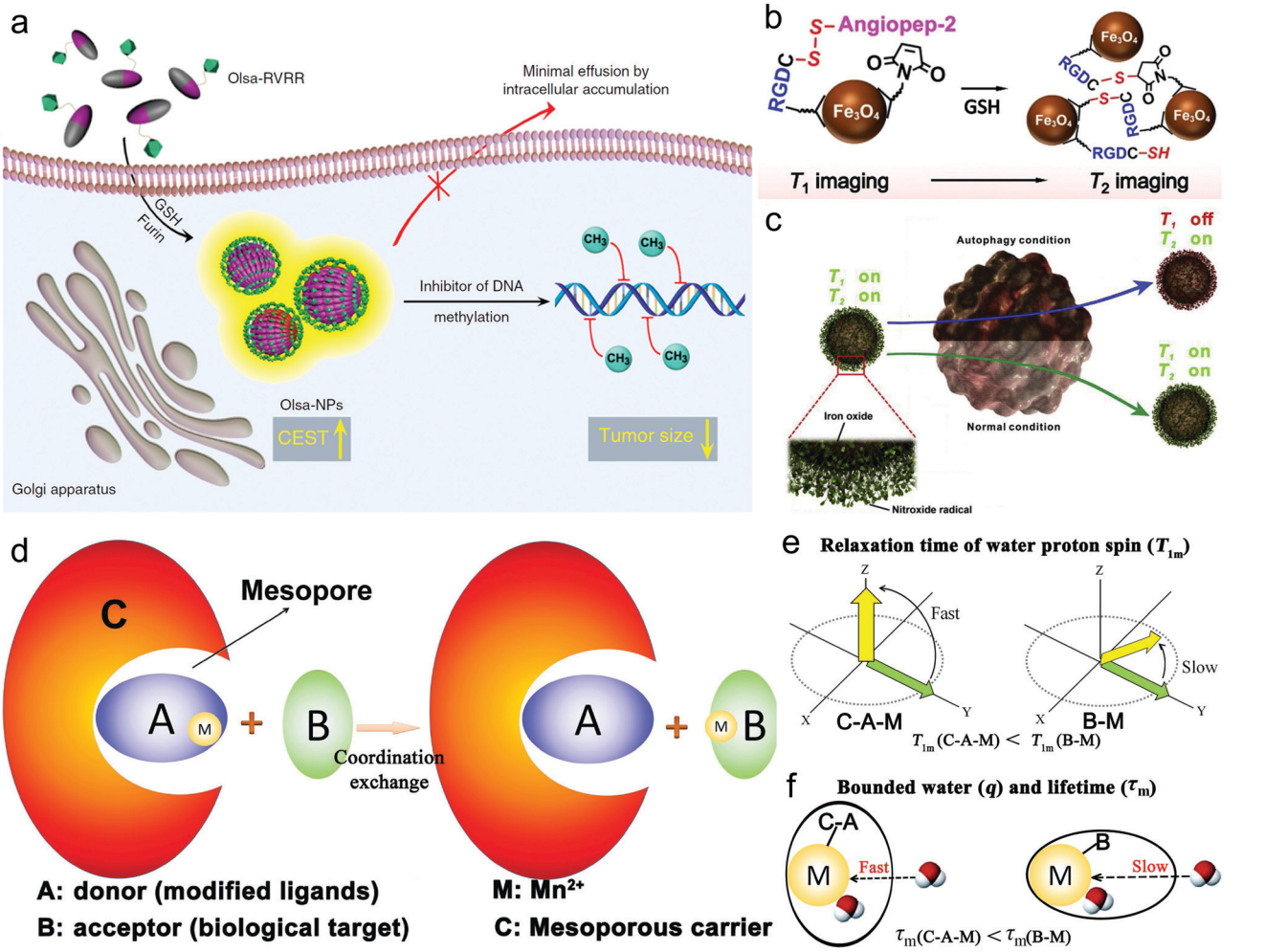

Fig. 8 (a) Schematic depicting the GSH and furin-responsive Olsa-RVRR cleavage and self-assembly for enhancing CEST and shrinking tumor in HCT116 cells that highly expressed furin. Reproduced with permission from ref. 110. Copyright 2019, Springer Nature. (b) Schematic depictions on the principle of GSH-activated probe aggregation for enhancing *T2*-MRI. Reproduced with permission from ref. 113. Copyright 2021, Wiley-VCH. (c) Schematic showing how Fe_3O_4–$NO^{\bullet}$ probe monitors ROS and reflects autophagy. Reproduced with permission from ref. 123. Copyright 2018, Elsevier Ltd. (d) Schematic to shed light on the CSRT strategy. Schematic on the relaxation time of water proton spin (e) and the bonded number of water and the exchange lifetime (f) in CRST strategy. Reproduced with permission from ref. 124. Copyright 2018, Wiley-VCH.

Their levels decide the different application categories, *e.g.*, tissue repairment or regeneration, tumor treatment, and inflammation alleviation. Considering this, elevating, reducing or sustaining the levels of ROS or reactive nitrogen species (RNS) has been harnessed using different methods (*e.g.*, PDT, CDT, SDT, GSH synthesis inhibition, GSH depletion and nanoenzyme-mediated ROS scavenging) to target these different applications,[119,120] which inevitably demand the precise monitoring of ROS or RNS. MRI also provides a candidate for tracing the reactive species. Autophagy plays an extraordinary role in tumor progression by selectively removing damaged organelles under cellular stress, indicating that the *in vivo* readout of autophagy is of great significance to illustrate the therapeutic and fundamental effect.[121,122] Intriguingly, tracking cellular stress can monitor the autophagy flux. Therefore, Zhang *et al.* synthesized $NO^{\bullet}$ radical-conjugated Fe_3O_4 nanoparticles (Fe_3O_4–$NO^{\bullet}$ NPs), acting as a dual-modal CA capable of analyzing autophagy dynamics under MR guidance.[123] In their investigation, the onset of autophagy causing the mass production of ROS would quench the $NO^{\bullet}$-induced *T*1-weighted signal, whereas the *T*2-weighted signal was condition-insensitive and remained constant due to the stability of the Fe_3O_4 nanoparticles upon autophagy, as shown in Fig. 8c. Therefore, the *T*1-signal variation could reflect the ROS level in a quantitative manner by benchmarking the *T*2-weighted signal in the autophagy dynamics.

Our group established a coordination-substitution-based relaxation tuning (CSRT) strategy for monitoring disease targets,[124] and its principle was shown in Fig. 8d. In detail, as Mn^{2+}-containing MRI CAs (C–A–M) touched biological targets (B), Mn^{2+} (M) ions were captured *via* coordination exchange by B to generate B–M (Fig. 8d), resulting in alterations in the water proton spin relaxation time and the number of bonded water protons and proton residence lifetime compared to C–A–M (Fig. 8e and f). By utilizing CSRT and designing the corresponding MRI CAs (C–A–M), GSH and hyaluronic acid (HA) were successfully detected and mapped.

Hypoxia is a specific hallmark of tumor progression, emerging in most solid tumors. It also severely resists ROS-based anti-tumor methods, *e.g.*, chemotherapy, SDT, PDT, and CDT, and thus great efforts have been devoted to alleviating hypoxia and improve anti-tumor outcomes.[120,125] In this regard, mapping hypoxia and detecting its level are also important for predicting tumor progression and evaluating curative and prognostic effects. Gregorio *et al.* utilized red blood cells (RBC) as vehicles to simultaneously conjugate with Gd-DOTP and Gd-HPDO3A, wherein Gd-DOTP and Gd-HPDO3A served as a hypoxia-responsive agent and RBC concentration reporter.[126] Relying on the hypoxia-activated longitudinal relaxation variation, these biomimetic probes were equipped with the ability to map hypoxia in a xenografted tumor-bearing mouse model.

Neural activity is closely correlated with intracellular calcium ions, and thus monitoring calcium ions is of great importance for assessing Ca^{2+} abnormality-related nerve diseases, similar to the aforementioned abnormal electric discharging. Alan Jasanoff *et al.* synthesized ManICS1-acetomethoxyl MRI CAs.[127] After entering cells, these MRI CAs underwent esterase cleavage, eventually enabling intracellular calcium levels to be monitored by MRI. As shown in Fig. 9a, the entrance of MRI CAs into cells led to the cleavage of AM esters, further liberating the calcium-free "off" state and eliciting a low MRI signal. Upon binding with calcium ions, the MRI signal could be enhanced again due to the blockade interactions between BAPTA and the paramagnetic platform. Besides monitoring the dynamic level of Ca^{2+}, neural stem cell (NSC) tracking is also favorable for evaluating the repairing progression of structural and functional damage after stroke and predicting the prognosis by co-delivering SPIONs and small interfering RNA/antisense oligonucleotides (siRNA/ASO) against Pnky long noncoding RNA (lncRNA) (Fig. 9b).[128] In detail, *in vivo* histologic analysis revealed that the neuronal differentiation (red) of the green fluorescence protein (GFP)-NSCs (green) indeed occurred at the transplantation site in stroke mice at 2 and 4 weeks after receiving Pnky-SPIO-PALC- or SCR-SPIO-PALC-transfected GFP-NSCs (Fig. 9c). Based on the cerebral infarct volume measured in the *T*2-weighted images, this multifunctional nanomedicine targeting lncRNA harvested a considerably-elevated treatment outcome in shrinking the cerebral infarct volume over time (Fig. 9d).

4.6 TME-activatable relaxation tuning for therapeutic gas monitoring

Gas therapy is another cancer therapeutic modality that utilizes gaseous molecules (*e.g.*, carbon monoxide (CO), nitric oxide (NO), and hydrogen sulfide (H_2S)) to elicit a therapeutic effect with negligible side effects.[129–131] Nevertheless, the precise delivery and controllable release of these therapeutic gases are still challenging, indicating that imaging-guided gas therapy is desirable and urgently demanded. Wu *et al.*[132] proposed a "TME remodeling" strategy, which could achieve the controllable and *in situ* release of CO. As reported in their research, the decomposition of manganese carbonyl could be caused by acidic TME remodeling, under which the H_2O_2-enriched TME could also stimulate CO gas release and paramagnetic Mn^{2+} ion generation for enhancing *T*1-weighted MRI. Therefore, the treatment process could be real-time monitored by *T*1-weighted MRI, avoiding the undesirable CO leakage.

H_2S plays an important role in various physiological and pathological processes, thereby arousing interest in qualitative and quantitative detection techniques for assessing the H_2S level *in vivo*. Based on the fact that Cu_2O can *in situ* respond to endogenous H_2S in colon tumors, Yan's group[71] constructed a core-shell-structured MRI/PAI dual-modal probe (Fe_3O_4@Cu_2O) for the detection of H_2S. In detail, the outer Cu_2O shell could adsorb H_2S on its surface, thus decreasing the distance between hydrogen protons and Fe, which resulted in a *T*1-weighted MRI enhancement, consequently visualizing H_2S in colorectal cancer. Similarly, a new type of FeS@BSA nanoclusters for MRI-guided synergetic tumor therapy was fabricated.[133] In the acidic TME, the FeS@BSA nanoclusters degraded to simultaneously release H_2S gas and Fe^{2+}, where the released Fe^{2+} not only could

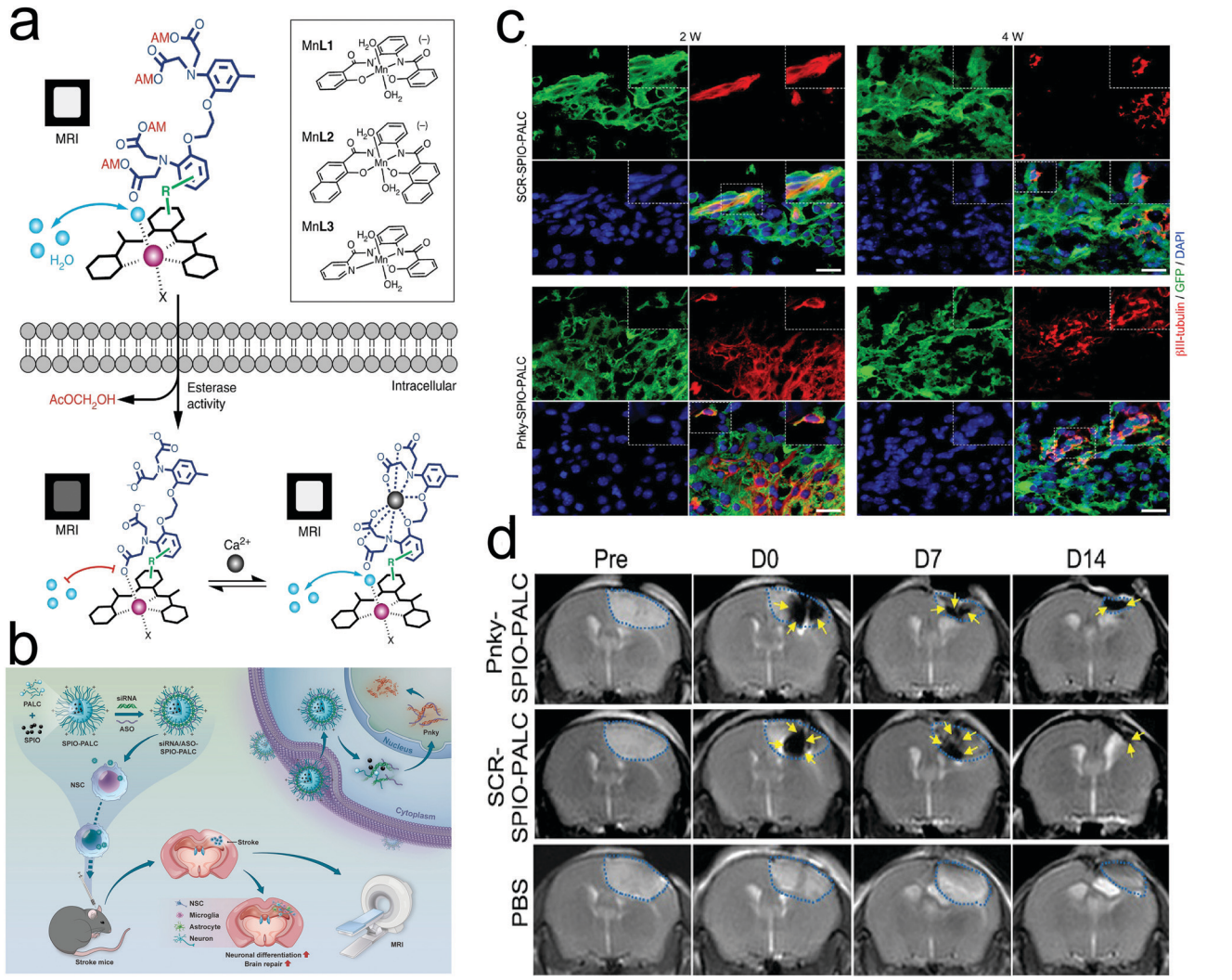

Fig. 9 (a) Design of cell-permeable sensors for calcium-dependent molecular fMRI. Reproduced with permission from ref. 127. Copyright 2019, Springer Nature. (b) Schematic depicting the directed neuronal differentiation of transplanted NSCs by silencing Pnky lncRNA and MRI tracking of NSCs in a mouse stroke model. (c) Confocal micrographs showing neuronal differentiation (red) of GFP-NSCs (green) in the transplantation site in stroke mice at 2 and 4 weeks. (d) Coronal *T*2-weighted MR images of stroke mice transplanted with Pnky-SPIO-PALC- or SCRSPIO-PALC-transfected NSCs and stroke mice. Reproduced with permission from ref. 128. Copyright 2021, the American Chemical Society.

induce ROS production effectively *via* Fenton reaction, but also enhance the on-site *T*2-weighted MRI signals.

4.7 Activatable MRI for tracking cell trajectory and change

Due to the high spatial resolution, inherent soft-tissue contrast and ion-free radiation, MRI is a promising visualization tool that has been utilized to qualitatively track large numbers of cells *in vivo*,[134] among which immune effector cells and immunosuppressive cells are highlighted because their distribution and infiltration directly decide the success or failure of anti-tumor immunotherapy.[135–137] Luo *et al.* developed a bioactivated *in vivo* assembly method and synthesized a CD206-targeting molecular MRI probe with cathepsin B-sensitive linker. As the probe entered macrophages, the intracellular cathepsin B degraded the linker and induced the probe to assemble into nanofibers with enhanced *T*1-weighted MRI, which allowed the real-time tracking of macrophage migration (Fig. 10a).[138] In another study that focused on dendritic cell (DCs)-activating magnetic nanoparticles,[139] researchers revealed that the inclusion of iron oxide could improve DC transfection, and also enable tracking the migration of DCs with MRI. As illustrated in Fig. 10b, researchers successfully fabricated ^{a}IO-RNA-NPs by combining IONPs and mRNA encoding tumor antigens in translated lipids. In the presence or absence of a magnetic field, the co-incubation of ^{a}IO-RNA-NPs with DCs resulted in profound DC activation and enabled the MRI-based detection of DC migration. In brief, this nanoplatform furnished a powerful tool to activate DCs and predict individual treatment responses to DC vaccines before tumor progression-related signs emerge. Furthermore, myeloid cells including immunosuppressive myeloid-derived suppressor cells (MDSCs) were also successfully tracked using ^{19}F MRI after developing the corresponding CAs.[140]

Stem cells are prevalent in damage repair, indicating that monitoring the viability, migration, homing and differentiation

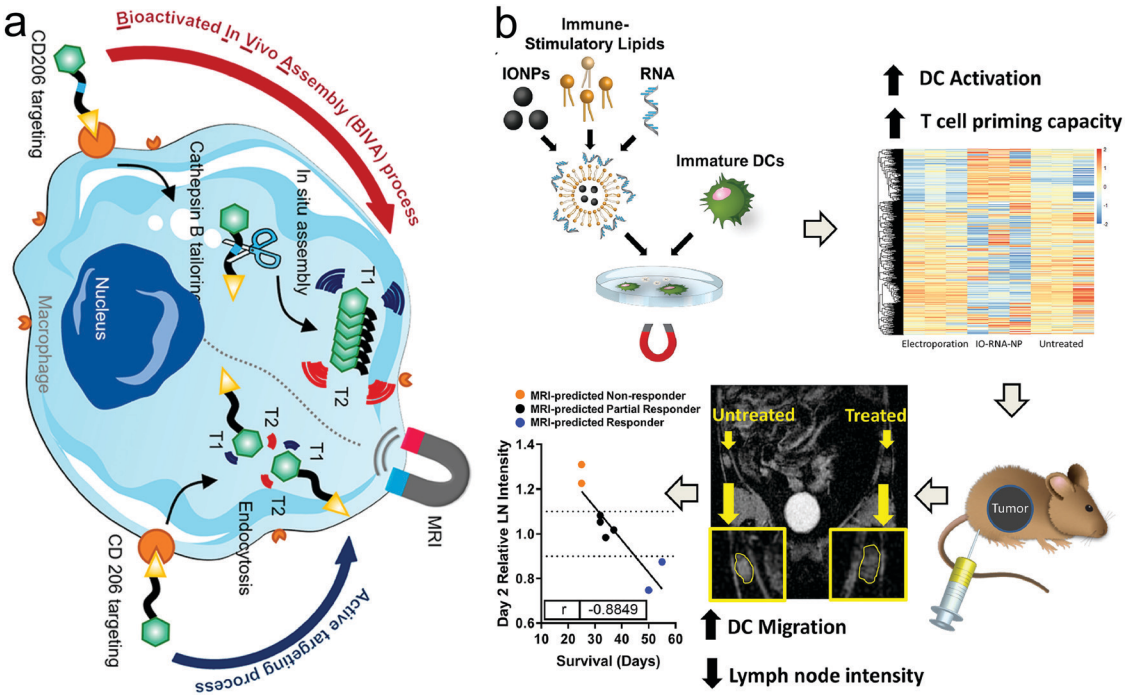

Fig. 10 (a) Schematic showing the principle of the bioactivated *in vivo* assembly method. Reproduced with permission from ref. 138. Copyright 2022, the American Chemical Society. (b) Schematic illustration of ^{a}IO-RNA-NPs. Reproduced with permission from ref. 139. Copyright 2019, the American Chemical Society.

of stem cells is of importance. The NIR-FLI/MRI dual-modal imaging-guided tracking of labeled mesenchymal stem cells in the brain of a mouse photothrombotic stroke model was reported to achieve noninvasive and real-time tracking for up to 14 days.[141] To reveal the *in vivo* fates of stem cell transplants, which is a promising treatment option for brain injuries, Deng

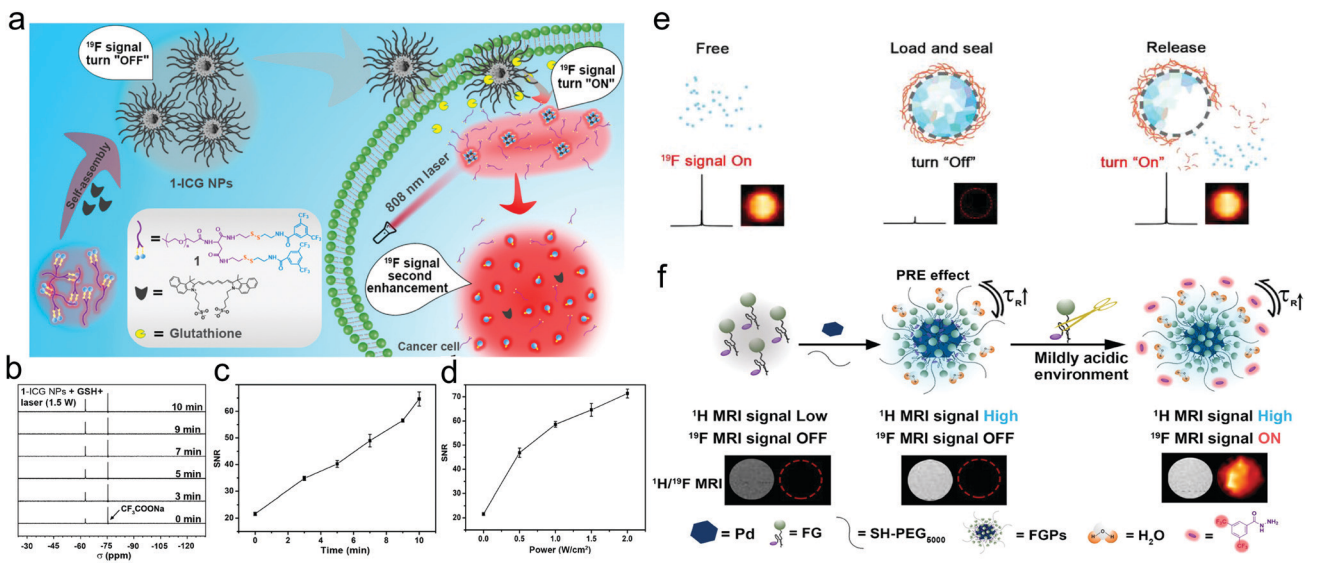

Fig. 11 (a) Schematic illustration of self-assembled multi-responsive probes for cascaded ^{19}F signal activation/amplification. (b) ^{19}F NMR spectra of 1-ICG nanoparticles in 500 μL of 10% D_2O/H_2O (after incubation with GSH for 2 h) upon 808 nm laser irradiation. (c) SNRs of ^{19}F NMR of 1-ICG nanoparticles in 500 μL of 10% D_2O/H_2O (after incubation with GSH for 2 h) upon 808 nm laser irradiation. (d) SNRs of ^{19}F NMR of 1-ICG nanoparticles (1368 μM; ICG, 21 μg mL^{-1}) with 808 nm laser irradiation at different power intensities for 10 min after incubation with GSH for 2 h. Reproduced with permission from ref. 146. Copyright 2020, the American Chemical Society. (e) Schematic illustration of FILAMP for stimuli-responsive ^{19}F MRI. Reproduced with permission from ref. 147. Copyright 2020, Elsevier. (f) Schematic illustration of fluorinated gadolinium chelate-grafted nanoconjugates for contrast-enhanced *T*1-weighted ^{1}H and pH-activatable ^{19}F dual-modal MRI. Reproduced with permission from ref. 148. Copyright 2020, the American Chemical Society.

et al. constructed a *T*2 MRI CA for labeling transplanted stem cells *via* electroporation.[142] As exocytosis or cell death occurred, the released MRI CAs could induce a signal enhancement in the surrounding tissue, and thus the labeled cells could be distinguished from hot tissue, concurrently providing abundant information on the *in vivo* fates of stem cell transplants.

Specific molecular MRI probes enable the characterization and visualization of molecular and cellular processes in diseases, thereby enhancing the therapeutic effect and monitoring disease progression, *e.g.*, thrombosis.[143] In a preclinical study, MRI uncovered the presence of multiple brain metastases in 15 patients bearing melanoma, lung cancer, colon cancer, and breast cancer in the first-in-human phase 1 clinical trial that received a single intravenous administration of Gd-based AGuIX nanoparticles.[144] The diagnostic value of Gd-based AGuIX nanoparticles for detecting brain metastases was measured to be equivalent to that of commercial clinically used CAs.

4.8 Activatable ^{19}F-based nanoprobe for MRI and target detection

As stated above, ^{19}F is an exceptional complement to ^{1}H in MRI given that it has relatively high sensitivity, low biological background, and broad chemical shift range compared with other competitors. Modulating the relaxation of ^{19}F nuclei is the major design strategy of ^{19}F MRI nanoprobes. As stated above, the ^{19}F sources that can be utilized in ^{19}F MRI include perfluorocarbons (PFCs), trifluoromethyl compounds, fluorinated ionic liquids, and other fluorine-containing compounds.[145] Tang *et al.*[146] synthesized a cascaded multi-responsive ^{19}F-bearing nanoprobe, where the ^{19}F signals could be firstly activated in the reducing TME, and subsequently the photothermal process could amplify the signal (Fig. 11a). The experimental results indicated that the external NIR light irradiation treatment indeed led to higher and sharper ^{19}F nuclear magnetic resonance (NMR) peaks (Fig. 11b) and elevated SNR as the irradiation time or the power density increased (Fig. 11c and d). *In vitro* and *in vivo* imaging

Table 1 Summary of types of stimulations and the responsive triggers together with the changes upon exposure to the related stimuli

Nanocomplex	MRI CAs	Trigger	Responsive mechanism	Ref.
$NaGdF_4$&$CaCO_3$-*co*-loaded nanospheres	*T*1 (Gd^{3+})	Endogenous pH (acidity)	Acid-activated release of Gd^{3+} due to the disintegration of $NaGdF_4$	97
Gd(III)-based probe 2 (PCP-2).	*T*1 (Gd^{3+})	Endogenous GSH	GSH-mediated self-assembly into nanoaggregates	150
P-CyFF-Gd	*T*1 (Gd^{3+})	Endogenous alkaline phosphatase (ALP) enzyme	ALP enzyme-responsive particle aggregation.	151
P-FFGd-TCO	*T*1 (Gd^{3+})	Endogenous ALP enzyme	ALP enzyme-responsive particle self-assembly	152
MSNs-PEG	*T*1 (Gd $(DTPA)^{2-}$)	Exogenous high-intensity focused ultrasound (HIFU)	HIFU stimulation cleave PEG shedding and Gd $(DTPA)^{2-}$ release	153
Electrically responsive hybrid micelle (EM)	*T*1 (Gd^{3+}-DTPA, USPIO)	Exogenous electric field	External electric field triggered particle disintegration	106
DNA–Mn hybrid nanoflower (DMNF)	*T*1 (Mn^{2+})	Endogenous pH (acidity)	Acid-activated release Mn^{2+}	154
SiO_2@Au@MnO_2–DOX/Apt	*T*1 (Mn^{2+})	Endogenous GSH	GSH-mediated MnO_2 decomposition and Mn^{4+} reduction into Mn^{2+}	155
DOX/MnO_2@PVCL NGs	*T*1(Mn^{2+})	Endogenous GSH	GSH-triggered Mn^{2+} release	156
Mesoporous Cu/Mn_2SiO_3 nanospheres (mCMSNs)	*T*1 (Mn^{2+})	Endogenous GSH	GSH-triggered mCMSNs degradation and Mn^{2+} release.	157
DL-Menthol (DLM)@Fe_3O_4	*T*1 (Fe_3O_4)	Exogenous radiofrequency ablation	DLM-induced inertial cavitation cooperated with Fe_3O_4-mediatd magnetothermal transformation	74
USPION-DOX nanovesicles (USD NVs)	*T*1 (USPIONs)	Endogenous GSH	GSH-responsive USPIO particles disaggregation	158
IONPs	*T*2 (Fe_3O_4)	Endogenous matrix metalloproteinase (MMP) enzymes	MMP enzymes-responsive self-assembled superparamagnetic nanocluster network	95
Chlorin e6 (Ce6) & Fe_3O_4-*co*-loaded polymeric micelles (Ce6/Fe_3O_4-M)	*T*2 (Fe_3O_4)	Exogenous PDT-provoked singlet oxygen	Singlet oxygen shortened the transverse relaxation time (*T*2)	159
Cystamine dihydrochloride (Cys) connected USPIO NPs	*T*2 to *T*1	Endogenous GSH	GSH-responsive USPIO NPs disintegrated and become monodispersed	98
USPIO NP-aggregated clusters entrapped in paramagnetic polymers	*T*2 to *T*1	Endogenous abnormal electric discharging during epilepsy seizure	Abnormal electric discharging widens the distance between polymer and clusters, restoring the *T*1 MRI signal	106
Co-encapsulating paramagnetic Mn^{2+} (P–Mn) chelates and SPIONs	*T*1 and *T*2	Endogenous GSH	GSH modulated the integrity of micelles and turned 'on' both *T*1 and *T*2 MRI signals	107
IONPs modified with HA	*T*1 and *T*2	Endogenous pH (acidity)	Acid-activated self-assembly of monodispersed IONPs	108
Fe_3O_4-NO$^{\bullet}$ NPs	*T*1 and *T*2	Endogenous autophagy	Endogenous autophagy quenches the *T*1-signal of NO$^{\bullet}$	123
^{19}F-bearing nanoprobe 1-ICG nanoparticles	^{19}F	Endogenous reducing TME External NIR light irradiation	Cascaded activated in the reducing TME and subsequently the photothermal process	146
Fluorinated ionic liquids (ILs)	^{19}F	Endogenous pH (acidity)	Acid-activated release of trapped ILs to switch on ^{19}F signal	147
Mn-LDH@PFPE nanoparticles	^{19}F&*T*1(Mn^{2+})	Endogenous pH (acidity)	Acid-activated release Mn^{2+} reduced the effect of paramagnetic relaxation	47

experiments also demonstrated the feasibility of ^{19}F signal activation/amplification in monitoring the reducing TEM and the photothermal process. Fluorinated ion liquids (ILs) is a new type of fluorine MRI CAs, which could be engineered into activatable ^{19}F MRI nanoplatforms.[147] Upon exposure to biological stimuli such as low pH, the ^{19}F signals would be obviously elevated given that the trapped ILs are released to switch on the ^{19}F signal (Fig. 11e). When acidity-activatable ^{19}F MRI was integrated with stable ^{1}H MRI in a MRI nanoconjugate, it provided a ratiometric dual-modal imaging probe for quantitatively detecting pH in tumors (Fig. 11f) using the pH-sensitive variation in the ^{19}F MRI signal as a pH indicator and ^{1}H MRI as the reference tag.[148]

Intriguingly, ^{19}F MRI could be also engineered into a theranostic nanoplatform capable of monitoring protease activity. As a paradigm, Ding and coworkers reported a protease-controlled strategy, which combined simultaneous $T2$ ^{1}H MRI enhancement and ^{19}F MRI "turn-on" effect in one nanoplatform when bridging an ^{19}F compound (*i.e.*, 4-(trifluoromethyl)benzoic acid (TFMB)-Arg-Val-Arg-Arg-Cys(StBu)-Lys-CBT) with Fe_3O_4.[149] Aggregation of Fe_3O_4 produced a stable $T2$-weighted ^{1}H MRI signal, while the detachment of the TFMB-ArgVal-Arg-Arg-OH residue from the nanocomplex in response to protease attenuated the paramagnetic relaxation enhancement (PRE) effect and turned on the ^{19}F MRI signal, enabling the detection of protease activity.

Taken together, it can be considered that "structure determines function" is one of the basic principles of designing new MRI modalities and corresponding MRI CAs. In general, the design strategy of novel MRI nanocomplexes is usually inspired by the bio-application demand and distinctive insight into the characteristics of nanomaterials. Various strategies for the stimuli-responsive triggered "on/off" effect were introduced, and the "on" and "off" states reflect the changes in the structure of MRI CAs induced by the disease environment, thereby enabling the detection of the disease environment including targets, biological activity and processes. We systematically illustrated the novel MRI modes reported to date in this review and we intend to exemplify the bio-applications of these strategies, hopefully establishing the relationship that bridges the structure of MRI-based CAs with the advantages of their application. Herein, we present a simple summary on the responsive triggers and the used mechanisms as well as the composition and structure of the corresponding MRI CA in Table 1.

5 Summary and future perspectives

In this review, we summarized the recent advances on $T1$ and $T2$ relaxation tuning with emphasis on the design strategies of nanobiotechnology and corresponding MRI CAs after a simple introduction of the basic principle of MRI. Especially, we elucidated the design principles and clarified the advantages of these MRI modes and corresponding MRI CAs in disease theranostics with an in-depth discussion on bio-applications. This review can offer distinctive insights into the design strategies of nanobiotechnology and corresponding MRI CAs based on relaxation tuning for different scientific communities. It is also believed that the presented MRI-guided therapeutic strategies in this review will significantly contribute to tackling clinical problems with the help of materials science.

Although nanobiotechnology-enabled MRI modes have been deeply investigated with increasing interest, there are still obstacles preventing their further clinical application. Firstly, most procedures for the synthesis of nanocomplexes functioning as MRI CAs are uncontrollable and variable to some extent. Hence, researchers should make efforts to pursue stable and mature preparation methods that are greener, cheaper and easier to mass production. Nanobiotechnology development can furnish reliable tools and rationalize the design or synthesis of MRI CAs, where intelligently-responsive and resizable nanoparticles gradually become the mainstream trend to realize the goal of multi-functions. Secondly, although impressive progress in biomedical applications has been achieved, it is worth noting that most strategies are still in the proof-of-concept stage. The aim of most researchers is to attain disease cure in clinic, dictating that the translation from laboratory to clinic is of great significance. Thereby, it is vital to perform in-depth studies on the biodistribution, biocompatibility and interaction of MRI CAs with biological systems before their translation to clinical applications. Meanwhile, preclinical and clinical research should be urgently accelerated. Thirdly, during the past decade, the utilization of water-soluble fluoropolymers in biomedical applications has grown rapidly and ^{19}F MRI has been developed as a convenient diagnostic technique. Nevertheless, few fluoride-based MRI CAs have been systematically investigated in comparison to ^{1}H MRI CAs. When designing fluorinated nanocompounds for biological applications, the important safety concern should be considered, where chemically-stable fluorine-containing molecules without releasing polyfluoroalkyl substances in the environment and human body are preferable, and thus require meticulous exploration. Also, the imaging sensitivity needs to be elevated, where the introduction of paramagnetic units with a relaxation enhancement effect in the course of fluoride-based CA design is considered to further improve the imaging sensitivity. Finally, more attention and efforts are needed for the exploration of refractory diseases besides cancer.

Abbreviations

MRI	Magnetic resonance imaging
CAs	Contrast agents
SNR	Signal-to-noise ratio
SPIONs	Superparamagnetic iron oxide nanoparticles
GQD	Graphene quantum dots
PGQD	Paramagnetic GQD
PEG	Polyethylene glycol
DOX	Doxorubicin
Ce6	Chlorin e6
UMFNPs	Ultrasmall manganese ferrite nanoparticles
HSA	Human serum albumin
FBS	Fetal bovine serum
BSA	Bovine serum albumin

IONPs	Iron oxide nanoparticles
MMP	Metalloproteinase
LDH	Layered double hydroxide
USPIO NPs	Ultrasmall superparamagnetic iron oxide nanoparticles
HA	Hyaluronic acid
MRET	Magnetic resonance tuning
TMRET	Two-way MERT
NIR	Near-infrared
NMR	Nuclear magnetic resonance
PRE	Paramagnetic relaxation enhancement
ALP	Alkaline phosphatase
HIFU	High-intensity focused ultrasound
GSH	Glutathione
CT	Computed tomography
PAI	Photoacoustic imaging
PET	Positron emission tomography
NIR-PL	Near-infrared persistent luminescence
PDT	Photodynamic therapy
SDT	Sonodynamic therapy
CDT	Chemodynamic therapy
PSs	Photosensitizers
CAT	Catalase
UCNPs	Upconversion nanoparticles
MHT	Magnetic hyperthermia therapy
AMF	Alternating magnetic field
RFA	Radiofrequency ablation
DLM	DL-Menthol
PTT	Photothermal therapy
P–Mn	Paramagnetic Mn^{2+}
EDTA	Ethylene diamine tetraacetic acid
RBC	Red blood cells
CO	Carbon monoxide
NO	Nitric oxide
H_2S	Hydrogen sulfide
TME	Tumor microenvironment
RNS	Reactive nitrogen species
ROS	Reactive oxygen species
DCs	Dendritic cells
NSCs	Neural stem cells
MDSCs	Myeloid-derived suppressor cells
GFP	Green fluorescence protein
CEST	Chemical exchange saturation transfer
CBT	2-Cyanobenzothiazole
TFMB	4-(Trifluoromethyl) benzoic acid
CSRT	Coordination-substitution-based relaxation tuning
FLI	Fluorescence imaging
PFCs	Perfluorocarbons
ITI	Infrared thermal imaging
NPs	Nanoparticles
ASO	Antisense oligonucleotides
ATO	Arsenic trioxide
MMP	Matrix metalloproteinase
Olsa	Olsalazine
CSRT	Coordination-substitution-based relaxation tuning
UCI	Ultrasound contrast imaging

Authors' contributions

K. Zhang and T. Wang conceived the theme, organized the structure and collect the references and materials. X. Zhang, Y. Xu, Y. Xu and Y. Zhang apply the copyright. T. Wang and K. Zhang wrote the paper, and K. Zhang revised manuscript and re-organized the figures.

Conflicts of interest

The authors declare no competing interests.

Acknowledgements

This work was supported by Outstanding Youth Fund of National Natural Science Foundation of China (No. 82022033), Shanghai Rising-Star Program (Grant No. 19QA1406800), Shanghai Talent Development Fund (Grant No. 2019040), the Fundamental Research Funds for the Central Universities (22120210561) and Shanghai Young Top-Notch Talent, National Natural Science Foundation of China (Grant No. 82171942) and Science and Technology Commission of Shanghai Municipality (Grant No. 20ZR1443400).

References

1 J. Kim, Y. Piao and T. Hyeon, *Chem. Soc. Rev.*, 2009, **38**, 372–390.
2 J. P. Liu, E. Fullerton, O. Gutfleisch and D. J. Sellmyer, *Nanoscale Magnetic Materials and Applications*, Springer, New York, NY, 2009, vol. 1.
3 B. Blasiak, F. C. J. M. van Veggel and B. Tomanek, *J. Nanomater.*, 2013, 1–12.
4 Y. A. Pirogov, *Phys. Procedia*, 2016, **82**, 3–7.
5 J. Wahsner, E. M. Gale, A. Rodriguez-Rodriguez and P. Caravan, *Chem. Rev.*, 2019, **119**, 957–1057.
6 M. Legacz, K. Roepke, M. Giersig and U. Pison, *Adv. Nanopart.*, 2014, **3**, 41–53.
7 Y.-K. Peng, S. C. E. Tsang and P.-T. Chou, *Mater. Today*, 2016, **19**, 336–348.
8 V. P. Grover, J. M. Tognarelli, M. M. Crossey, I. J. Cox, S. D. Taylor-Robinson and M. J. McPhail, *J. Clin. Exp. Hepatol.*, 2015, **5**, 246–255.
9 I. Tirotta, V. Dichiarante, C. Pigliacelli, G. Cavallo, G. Terraneo, F. B. Bombelli, P. Metrangolo and G. Resnati, *Chem. Rev.*, 2015, **115**, 1106–1129.
10 H. Matsushita, S. Mizukami, F. Sugihara, Y. Nakanishi, Y. Yoshioka and K. Kikuchi, *Angew. Chem., Int. Ed.*, 2014, **53**, 1008–1011.
11 R. Kumar, W. S. Shin, K. Sunwoo, W. Y. Kim, S. Koo, S. Bhuniya and J. S. Kim, *Chem. Soc. Rev.*, 2015, **44**, 6670–6683.
12 L. Jamgotchian, S. Vaillant, E. Selingue, A. Doerflinger, A. Belime, M. Vandamme, G. Pinna, W. L. Ling, E. Gravel, S. Meriaux and E. Doris, *Nanoscale*, 2021, **13**, 2373–2377.

13 J. Kim, N. Lee and T. Hyeon, *Philos. Trans. R. Soc., A*, 2017, **375**, 20170022.
14 J. K. Oh and J. M. Park, *Prog. Polym. Sci.*, 2011, **36**, 168–189.
15 K. Ulbrich, K. Hola, V. Subr, A. Bakandritsos, J. Tucek and R. Zboril, *Chem. Rev.*, 2016, **116**, 5338–5431.
16 Y. Xiao and J. Du, *J. Mater. Chem. B*, 2020, **8**, 354–367.
17 Y. Lin, K. Zhang, R. Zhang, Z. She, R. Tan, Y. Fan and X. Li, *J. Mater. Chem. B*, 2020, **8**, 5973–5991.
18 D. Weishaupt, V. D. Kochli, B. Marincek and E. E. Kim, *J. Nucl. Med.*, 2007, **48**, 1910.
19 S. Mastrogiacomo, W. Dou, J. A. Jansen and X. F. Walboomers, *Mol. Imaging Biol.*, 2019, **21**, 1003–1019.
20 Z. R. Stephen, F. M. Kievit and M. Zhang, *Mater. Today*, 2011, **14**, 330–338.
21 L. G. Hanson, *Concepts Magn. Reson., Part A*, 2008, **32A**, 329–340.
22 Y. D. Xiao, R. Paudel, J. Liu, C. Ma, Z. S. Zhang and S. K. Zhou, *Int. J. Mol. Med.*, 2016, **38**, 1319–1326.
23 D. Pan, A. H. Schmieder, S. A. Wickline and G. M. Lanza, *Tetrahedron*, 2011, **67**, 8431–8444.
24 N. A. Keasberry, M. Banobre-Lopez, C. Wood, G. J. Stasiuk, J. Gallo and N. J. Long, *Nanoscale*, 2015, **7**, 16119–16128.
25 B. H. Kim, N. Lee, H. Kim, K. An, Y. I. Park, Y. Choi, K. Shin, Y. Lee, S. G. Kwon, H. B. Na, J. G. Park, T. Y. Ahn, Y. W. Kim, W. K. Moon, S. H. Choi and T. Hyeon, *J. Am. Chem. Soc.*, 2011, **133**, 12624–12631.
26 R. Chen, A. Canales and P. Anikeeva, *Nat. Rev. Mater.*, 2017, **2**, 16093.
27 Y. Hu, S. Mignani, J. P. Majoral, M. Shen and X. Shi, *Chem. Soc. Rev.*, 2018, **47**, 1874–1900.
28 V. Gulani, F. Calamante, F. G. Shellock, E. Kanal and S. B. Reeder, *Lancet Neurol.*, 2017, **16**, 564–570.
29 T. J. Fraum, D. R. Ludwig, M. R. Bashir and K. J. Fowler, *J. Magn. Reson. Imaging*, 2017, **46**, 338–353.
30 Y. Yang, S. Chen, H. Li, Y. Yuan, Z. Zhang, J. Xie, D. W. Hwang, A. Zhang, M. Liu and X. Zhou, *Nano Lett.*, 2019, **19**, 441–448.
31 Y. Li, H. Dong, Q. Tao, C. Ye, M. Yu, J. Li, H. Zhou, S. Yang, G. Ding and X. Xie, *Biomaterials*, 2020, **250**, 120056.
32 J. G. Penfield and R. F. Reilly, Jr., *Nat. Clin. Pract. Nephrol.*, 2007, **3**, 654–668.
33 L. Henderson, O. Neumann, C. Kaffes, R. Zhang, V. Marangoni, M. K. Ravoori, V. Kundra, J. Bankson, P. Nordlander and N. J. Halas, *ACS Nano*, 2018, **12**, 8214–8223.
34 W. Xie, Z. Guo, Z. Cao, Q. Gao, D. Wang, C. Boyer, M. Kavallaris, X. Sun, X. Wang, L. Zhao and Z. Gu, *ACS Biomater. Sci. Eng.*, 2019, **5**, 2555–2562.
35 T. Sun, Y. Liu, C. Zhou, L. Zhang, X. Kang, S. Xiao, M. Du, Z. Xu, Y. Liu, G. Liu, M. Gong and D. Zhang, *Nanoscale*, 2021, **13**, 7638–7647.
36 P. Zhang, Y. Hou, J. Zeng, Y. Li, Z. Wang, R. Zhu, T. Ma and M. Gao, *Angew. Chem., Int. Ed.*, 2019, **58**, 11088–11096.
37 L. Palagi, E. Di Gregorio, D. Costanzo, R. Stefania, C. Cavallotti, M. Capozza, S. Aime and E. Gianolio, *J. Am. Chem. Soc.*, 2021, **143**, 14178–14188.
38 B. Chen, Z. Guo, C. Guo, Y. Mao, Z. Qin, D. Ye, F. Zang, Z. Lou, Z. Zhang, M. Li, Y. Liu, M. Ji, J. Sun and N. Gu, *Nanoscale*, 2020, **12**, 5521–5532.
39 R. Jin, B. Lin, D. Li and H. Ai, *Curr. Opin. Pharmacol.*, 2014, **18**, 18–27.
40 Z. Zhou, L. Yang, J. Gao and X. Chen, *Adv. Mater.*, 2019, **31**, 1804567.
41 C. Du, J. Wang, X. Liu, H. Li, D. Geng, L. Yu, Y. Chen and J. Zhang, *Biomaterials*, 2020, **230**, 119581.
42 N. Zhang, Y. Wang, C. Zhang, Y. Fan, D. Li, X. Cao, J. Xia, X. Shi and R. Guo, *Theranostics*, 2020, **10**, 2791–2802.
43 M. Ma, H. Zhu, J. Ling, S. Gong, Y. Zhang, Y. Xia and Z. Tang, *ACS Nano*, 2020, **14**, 4036–4044.
44 X. Xue, R. Bo, H. Qu, B. Jia, W. Xiao, Y. Yuan, N. Vapniarsky, A. Lindstrom, H. Wu, D. Zhang, L. Li, M. Ricci, Z. Ma, Z. Zhu, T. Y. Lin, A. Y. Louie and Y. Li, *Biomaterials*, 2020, **257**, 120234.
45 C. Zhang, K. Yan, C. Fu, H. Peng, C. J. Hawker and A. K. Whittaker, *Chem. Rev.*, 2022, **122**, 167–208.
46 J. Lv and Y. Cheng, *Chem. Soc. Rev.*, 2021, **50**, 5435–5467.
47 C. Zhang, L. Li, F. Y. Han, X. Yu, X. Tan, C. Fu, Z. P. Xu and A. K. Whittaker, *Small*, 2019, **15**, 1902309.
48 K. Zhang, H. Chen, P. Li, X. Bo, X. Li, Z. Zeng and H. Xu, *ACS Appl. Mater. Interfaces*, 2015, **7**, 18590–18599.
49 Z. Wang, J. Liu, T. Li, J. Liu and B. Wang, *J. Mater. Chem. B*, 2014, **2**, 4748–4753.
50 Y. Yong, L. Zhou, S. Zhang, L. Yan, Z. Gu, G. Zhang and Y. Zhao, *NPG Asia Mater.*, 2016, **8**, e273.
51 Z. Chen, Y. Peng, Y. Li, X. Xie, X. Wei, G. Yang, H. Zhang, N. Li, T. Li, X. Qin, S. Li, C. Wu, F. You, H. Yang and Y. Liu, *ACS Nano*, 2021, **15**, 16683–16696.
52 L. Xia, X. Meng, L. Wen, N. Zhou, T. Liu, X. Xu, F. Wang, Z. Cheng, Z. Yang and H. Zhu, *Small*, 2021, **17**, 2100378.
53 X. Han, Y. Xu, Y. Li, X. Zhao, Y. Zhang, H. Min, Y. Qi, G. J. Anderson, L. You, Y. Zhao and G. Nie, *ACS Nano*, 2019, **13**, 4379–4391.
54 S. M. Janib, A. S. Moses and J. A. MacKay, *Adv. Drug Delivery Rev.*, 2010, **62**, 1052–1063.
55 R. Zou, J. Li, T. Yang, Y. Zhang, J. Jiao, K. L. Wong and J. Wang, *Theranostics*, 2021, **11**, 8448–8463.
56 Z. Zeng, C. Fang, Y. Zhang, C.-X. Chen, Y.-F. Zhang and K. Zhang, *Front. Bioeng. Biotechnol.*, 2021, **9**, 784602.
57 L. Lei, S. Cai, Y. Zhang, L. Yang, J. Deng, H. Mei, X. Zhang, K. Zhang, B. He and J. Cao, *Adv. Funct. Mater.*, 2022, **32**, 2103394.
58 H. Mei, X. Zhang, S. Cai, X. Zhang, Y. Zhang, Z. Guo, W. Shi, R. Chu, K. Zhang, J. Cao and B. He, *Nano Today*, 2021, **41**, 101305.
59 R. An, X. Cheng, S. Wei, Y. Hu, Y. Sun, Z. Huang, H. Y. Chen and D. Ye, *Angew. Chem., Int. Ed.*, 2020, **59**, 20636–20644.
60 Y. Wang, Y. Li, Z. Zhang, L. Wang, D. Wang and B. Z. Tang, *Adv. Mater.*, 2021, **33**, 2103748.
61 H. Fan, G. Yan, Z. Zhao, X. Hu, W. Zhang, H. Liu, X. Fu, T. Fu, X. B. Zhang and W. Tan, *Angew. Chem., Int. Ed.*, 2016, **55**, 5477–5482.
62 T. Zhang, Z. Jiang, L. Chen, C. Pan, S. Sun, C. Liu, Z. Li, W. Ren, A. Wu and P. Huang, *Nano Res.*, 2020, **13**, 273–281.

63 J. Zhu, T. Xiao, J. Zhang, H. Che, Y. Shi, X. Shi and J. C. M. van Hest, *ACS Nano*, 2020, **14**, 11225–11237.
64 J. Xu, R. Shi, G. Chen, S. Dong, P. Yang, Z. Zhang, N. Niu, S. Gai, F. He, Y. Fu and J. Lin, *ACS Nano*, 2020, **14**, 9613–9625.
65 N. Wang, Q. Zeng, R. Zhang, D. Xing and T. Zhang, *Theranostics*, 2021, **11**, 2334–2348.
66 I. M. Obaidat, B. Issa and Y. Haik, *Nanomaterials*, 2015, **5**, 63–89.
67 M.-H. Chan, M.-R. Hsieh, R.-S. Liu, D.-H. Wei and M. Hsiao, *Chem. Mater.*, 2019, **32**, 697–708.
68 T. Kim, E. Momin, J. Choi, K. Yuan, H. Zaidi, J. Kim, M. Park, N. Lee, M. T. McMahon, A. Quinones-Hinojosa, J. W. Bulte, T. Hyeon and A. A. Gilad, *J. Am. Chem. Soc.*, 2011, **133**, 2955–2961.
69 Z. Li, P. W. Yi, Q. Sun, H. Lei, H. Li Zhao, Z. H. Zhu, S. C. Smith, M. B. Lan and G. Q. M. Lu, *Adv. Funct. Mater.*, 2012, **22**, 2387–2393.
70 C. Bai, Z. Jia, L. Song, W. Zhang, Y. Chen, F. Zang, M. Ma, N. Gu and Y. Zhang, *Adv. Funct. Mater.*, 2018, **28**, 1802281.
71 J. Shen, T. W. Rees, Z. Zhou, S. Yang, L. Ji and H. Chao, *Biomaterials*, 2020, **251**, 120079.
72 E. Ximendes, R. Marin, Y. Shen, D. Ruiz, D. Gomez-Cerezo, P. Rodriguez-Sevilla, J. Lifante, P. X. Viveros-Mendez, F. Gamez, D. Garcia-Soriano, G. Salas, C. Zalbidea, A. Espinosa, A. Benayas, N. Garcia-Carrillo, L. Cusso, M. Desco, F. J. Teran, B. H. Juarez and D. Jaque, *Adv. Mater.*, 2021, **33**, 2100077.
73 C. Yan, D. Liu, L. An, Y. Wang, Q. Tian, J. Lin and S. Yang, *Anal. Chem.*, 2020, **92**, 8254–8261.
74 Y. Fang, H.-Y. Li, H.-H. Yin, S.-H. Xu, W.-W. Ren, S.-S. Ding, W.-Z. Tang, L.-H. Xiang, R. Wu, X. Guan and K. Zhang, *ACS Appl. Mater. Interfaces*, 2019, **11**, 11251–11261.
75 K. Zhang, H. Y. Li, J. Y. Lang, X. T. Li, W. W. Yue, Y. F. Yin, D. Du, Y. Fang, H. Wu, Y. X. Zhao and C. Xu, *Adv. Funct. Mater.*, 2019, **29**, 1905124.
76 K. Zhang, H. Chen, F. Li, Q. Wang, S. Zheng, H. Xu, M. Ma, X. Jia, Y. Chen, J. Mou, X. Wang and J. Shi, *Biomaterials*, 2014, **35**, 5875–5885.
77 Y. Zhang, L. Guo, F. Kong, L. Duan, H. Li, C. Fang and K. Zhang, *Wiley Interdiscip. Rev.: Nanomed. Nanobiotechnol.*, 2021, **13**, e1733.
78 G. J. Stasiuk, H. Smith, M. Wylezinska-Arridge, J. L. Tremoleda, W. Trigg, S. K. Luthra, V. Morisson Iveson, F. N. Gavins and N. J. Long, *Chem. Commun.*, 2013, **49**, 564–566.
79 T. Ma, Y. Hou, J. Zeng, C. Liu, P. Zhang, L. Jing, D. Shangguan and M. Gao, *J. Am. Chem. Soc.*, 2018, **140**, 211–218.
80 K. Umezawa, M. Yoshida, M. Kamiya, T. Yamasoba and Y. Urano, *Nat. Chem.*, 2017, **9**, 279–286.
81 J. Jo, C. H. Lee, R. Kopelman and X. Wang, *Nat. Commun.*, 2017, **8**, 471.
82 Z. Geng, F. Chen, X. Wang, L. Wang, Y. Pang and J. Liu, *Biomaterials*, 2021, **275**, 120897.
83 S. Anbu, S. H. L. Hoffmann, F. Carniato, L. Kenning, T. W. Price, T. J. Prior, M. Botta, A. F. Martins and G. J. Stasiuk, *Angew. Chem., Int. Ed.*, 2021, **60**, 10736–10744.
84 B. Duan, D. Wang, H. Wu, P. Xu, P. Jiang, G. Xia, Z. Liu, H. Wang, Z. Guo and Q. Chen, *ACS Biomater. Sci. Eng.*, 2018, **4**, 3047–3054.
85 Y. Zhang, Y. Yin, W. Zhang, H. Li, T. Wang, H. Yin, L. Sun, C. Su, K. Zhang and H. Xu, *J. Nanobiotechnol.*, 2021, **19**, 161.
86 X. Qian, X. Han, L. Yu, T. Xu and Y. Chen, *Adv. Funct. Mater.*, 2019, **30**, 1907066.
87 V. S. Lelyveld, E. Brustad, F. H. Arnold and A. Jasanoff, *J. Am. Chem. Soc.*, 2011, **133**, 649–651.
88 M. Z. Koylu, S. Asubay and A. Yilmaz, *Molecules*, 2009, **14**, 1537–1545.
89 Y. Li, X. Zhao, X. Liu, K. Cheng, X. Han, Y. Zhang, H. Min, G. Liu, J. Xu, J. Shi, H. Qin, H. Fan, L. Ren and G. Nie, *Adv. Mater.*, 2020, **32**, 1906799.
90 P. Mi, D. Kokuryo, H. Cabral, H. Wu, Y. Terada, T. Saga, I. Aoki, N. Nishiyama and K. Kataoka, *Nat. Nanotechnol.*, 2016, **11**, 724–730.
91 T. Hyeon, *Chem. Commun.*, 2003, 927–934, DOI: **10.1039/b207789b**.
92 N. Tran and T. J. Webster, *J. Mater. Chem.*, 2010, **20**, 8760–8767.
93 C. Kaittanis, S. A. Naser and J. M. Perez, *Nano Lett.*, 2006, **7**, 380–383.
94 Q. Wang, Z. Liang, F. Li, J. Lee, L. E. Low and D. Ling, *Exploration*, 2021, **1**, 20210009.
95 J. Gallo, N. Kamaly, I. Lavdas, E. Stevens, Q. D. Nguyen, M. Wylezinska-Arridge, E. O. Aboagye and N. J. Long, *Angew. Chem., Int. Ed.*, 2014, **53**, 9550–9554.
96 A. Shen, X. Meng, X. Gao, X. Xu, C. Shao, Z. Tang, Y. Liu, W. Bu and P. Wang, *Adv. Funct. Mater.*, 2019, **29**, 1803832.
97 Z. Yi, Z. Luo, N. D. Barth, X. Meng, H. Liu, W. Bu, A. All, M. Vendrell and X. Liu, *Adv. Mater.*, 2019, **31**, 1901851.
98 D. Ma, M. Shi, X. Li, J. Zhang, Y. Fan, K. Sun, T. Jiang, C. Peng and X. Shi, *Bioconjugate Chem.*, 2020, **31**, 352–359.
99 X. Zhu, J. Li, P. Peng, N. Hosseini Nassab and B. R. Smith, *Nano Lett.*, 2019, **19**, 6725–6733.
100 Z. Zhao, X. Wang, Z. Zhang, H. Zhang, H. Liu, X. Zhu, H. Li, X. Chi, Z. Yin and J. Gao, *ACS Nano*, 2015, **9**, 2749–2759.
101 S. Ren, J. Yang, L. Ma, X. Li, W. Wu, C. Liu, J. He and L. Miao, *ACS Appl. Mater. Interfaces*, 2018, **10**, 31947–31958.
102 F. Li, D. Zhi, Y. Luo, J. Zhang, X. Nan, Y. Zhang, W. Zhou, B. Qiu, L. Wen and G. Liang, *Nanoscale*, 2016, **8**, 12826–12833.
103 Z. Zhou, D. Huang, J. Bao, Q. Chen, G. Liu, Z. Chen, X. Chen and J. Gao, *Adv. Mater.*, 2012, **24**, 6223–6228.
104 D. W. Yoo, J.-H. Lee, T.-H. Shin and A. J. Cheon, *Acc. Chem. Res.*, 2011, **44**, 863–874.
105 J. S. Choi, S. Kim, D. Yoo, T. H. Shin, H. Kim, M. D. Gomes, S. H. Kim, A. Pines and J. Cheon, *Nat. Mater.*, 2017, **16**, 537–542.
106 C. Wang, W. Sun, J. Zhang, J. Zhang, Q. Guo, X. Zhou, D. Fan, H. Liu, M. Qi, X. Gao, H. Xu, Z. Gao, M. Tian, H. Zhang, J. Wang, Z. Wei, N. J. Long, Y. Mao and C. Li, *Nat. Biomed. Eng.*, 2021, **5**, 278–289.
107 Z. Wang, X. Xue, H. Lu, Y. He, Z. Lu, Z. Chen, Y. Yuan, N. Tang, C. A. Dreyer, L. Quigley, N. Curro, K. S. Lam,

J. H. Walton, T. Y. Lin, A. Y. Louie, D. A. Gilbert, K. Liu, K. W. Ferrara and Y. Li, *Nat. Nanotechnol.*, 2020, **15**, 482–490.

108 C. Pan, J. Lin, J. Zheng, C. Liu, B. Yuan, O. U. Akakuru, M. Zubair Iqbal, Q. Fang, J. Hu, J. Chen, J. Lin, Q. Dai, X. Guo, Z. Li, T. Zhang, C. Xu, X. Ma, T. Chen, A. Wu and Y. Jin, *Nanoscale*, 2021, **13**, 6461–6474.

109 K. M. Ward, A. H. Aletras and R. S. Balaban, *J. Magn. Reson.*, 2000, **143**, 79–87.

110 Y. Yuan, J. Zhang, X. Qi, S. Li, G. Liu, S. Siddhanta, I. Barman, X. Song, M. T. McMahon and J. W. M. Bulte, *Nat. Mater.*, 2019, **18**, 1376–1383.

111 Z. Ren, S. Sun, R. Sun, G. Cui, L. Hong, B. Rao, A. Li, Z. Yu, Q. Kan and Z. Mao, *Adv. Mater.*, 2020, **32**, 1906024.

112 Z. Sha, S. Yang, L. Fu, M. Geng, J. Gu, X. Liu, S. Li, X. Zhou and C. He, *Nanoscale*, 2021, **13**, 5077–5093.

113 P. Zhang, J. Zeng, Y. Li, C. Yang, J. Meng, Y. Hou and M. Gao, *Angew. Chem., Int. Ed.*, 2021, **60**, 8130–8138.

114 E. M. R. Lake, X. Ge, X. Shen, P. Herman, F. Hyder, J. A. Cardin, M. J. Higley, D. Scheinost, X. Papademetris, M. C. Crair and R. T. Constable, *Nat. Methods*, 2020, **17**, 1262–1271.

115 M. Yang, Y. Zhang, C. Fang, L. Song, Y. Wang, L. Lu, R. Yang, Z. Bu, X. Liang, K. Zhang and Q. Fu, *Adv. Mater.*, 2022, **34**, 2109522.

116 L. Zheng, S. Liu, X. Cheng, Z. Qin, Z. Lu, K. Zhang and J. Zhao, *Adv. Sci.*, 2019, **6**, 1900099.

117 K. Zhang, Y. Fang, Y. He, H. Yin, X. Guan, Y. Pu, B. Zhou, W. Yue, W. Ren, D. Du, H. Li, C. Liu, L. Sun, Y. Chen and H. Xu, *Nat. Commun.*, 2019, **10**, 5380.

118 H. Cao, L. Duan, Y. Zhang, J. Cao and K. Zhang, *Signal Transduction Targeted Ther.*, 2021, **6**, 426.

119 X. Guan, H.-H. Yin, X.-H. Xu, G. Xu, Y. Zhang, B.-G. Zhou, W.-W. Yue, C. Liu, L.-P. Sun, H.-X. Xu and K. Zhang, *Adv. Funct. Mater.*, 2020, **30**, 2000326.

120 T. Luo, D. Wang, L. Liu, Y. Zhang, C. Han, Y. Xie, Y. Liu, J. Liang, G. Qiu, H. Li, D. Su, J. Liu and K. Zhang, *Adv. Sci.*, 2021, **8**, 2101065.

121 C. He and D. J. Klionsky, *Annu. Rev. Genet.*, 2009, **43**, 67–93.

122 L. Robke, L. Laraia, M. A. Carnero Corrales, G. Konstantinidis, M. Muroi, A. Richters, M. Winzker, T. Engbring, S. Tomassi, N. Watanabe, H. Osada, D. Rauh, H. Waldmann, Y. W. Wu and J. Engel, *Angew. Chem., Int. Ed.*, 2017, **56**, 8153–8157.

123 C. Zhang, J. Ren, J. He, Y. Ding, D. Huo and Y. Hu, *Biomaterials*, 2018, **179**, 186–198.

124 K. Zhang, Y. Cheng, W. Ren, L. Sun, C. Liu, D. Wang, L. Guo, H. Xu and Y. Zhao, *Adv. Sci.*, 2018, **5**, 1800021.

125 J. Chen, H. Luo, Y. Liu, W. Zhang, H. Li, T. Luo, K. Zhang, Y. Zhao and J. Liu, *ACS Nano*, 2017, **11**, 12849–12862.

126 E. D. Gregorio, G. Ferrauto, E. Gianolio, S. Lanzardo, C. Carrera, F. Fedeli and S. Aime, *ACS Nano*, 2015, **9**, 8239–8248.

127 A. Barandov, B. B. Bartelle, C. G. Williamson, E. S. Loucks, S. J. Lippard and A. Jasanoff, *Nat. Commun.*, 2019, **10**, 897.

128 B. Lin, L. Lu, Y. Wang, Q. Zhang, Z. Wang, G. Cheng, X. Duan, F. Zhang, M. Xie, H. Le, X. Shuai and J. Shen, *Nano Lett.*, 2021, **21**, 806–815.

129 Y. Liu, F. Yang, C. Yuan, M. Li, T. Wang, B. Chen, J. Jin, P. Zhao, J. Tong, S. Luo and N. Gu, *ACS Nano*, 2017, **11**, 1509–1519.

130 X. Jia, Y. Zhang, Y. Zou, Y. Wang, D. Niu, Q. He, Z. Huang, W. Zhu, H. Tian, J. Shi and Y. Li, *Adv. Mater.*, 2018, **30**, 1704490.

131 P. Zhao, Z. Jin, Q. Chen, T. Yang, D. Chen, J. Meng, X. Lu, Z. Gu and Q. He, *Nat. Commun.*, 2018, **9**, 4241.

132 J. Wu, Z. Meng, A. A. Exner, X. Cai, X. Xie, B. Hu, Y. Chen and Y. Zheng, *Biomaterials*, 2021, **276**, 121001.

133 C. Xie, D. Cen, Z. Ren, Y. Wang, Y. Wu, X. Li, G. Han and X. Cai, *Adv. Sci.*, 2020, **7**, 1903512.

134 W. J. Rogers, C. H. Meyer and C. M. Kramer, *Nat. Clin. Pract. Cardiovasc. Med.*, 2006, **3**, 554–562.

135 J. Zhang, M. Yang, X. Fan, M. Zhu, Y. Yin, H. Li, J. Chen, S. Qin, H. Zhang, K. Zhang and F. Yu, *J. Nanobiotechnol.*, 2022, **20**, 103.

136 Y. Yin, X. Jiang, L. Sun, H. Li, C. Su, Y. Zhang, G. Xu, X. Li, C. Zhao, Y. Chen, H. Xu and K. Zhang, *Nano Today*, 2021, **36**, 101009.

137 H. Wu, H. Li, Y. Liu, J. Liang, Q. Liu, Z. Xu, Z. Chen, X. Zhang, K. Zhang and C. Xu, *Bioact. Mater.*, 2022, **13**, 223–238.

138 L.-J. Luo, X.-M. Liu, X. Zhang, J. Liu, Y. Gao, T.-Y. Sun and L.-L. Li, *Nano Lett.*, 2022, **22**, 1694–1702.

139 A. J. Grippin, B. Wummer, T. Wildes, K. Dyson, V. Trivedi, C. Yang, M. Sebastian, H. R. Mendez-Gomez, S. Padala, M. Grubb, M. Fillingim, A. Monsalve, E. J. Sayour, J. Dobson and D. A. Mitchell, *ACS Nano*, 2019, **13**, 13884–13898.

140 M. L. Senders, A. E. Meerwaldt, M. M. T. van Leent, B. L. Sanchez-Gaytan, J. C. van de Voort, Y. C. Toner, A. Maier, E. D. Klein, N. A. T. Sullivan, A. M. Sofias, H. Groenen, C. Faries, R. S. Oosterwijk, E. M. van Leeuwen, F. Fay, E. Chepurko, T. Reiner, R. Duivenvoorden, L. Zangi, R. M. Dijkhuizen, S. Hak, F. K. Swirski, M. Nahrendorf, C. Perez-Medina, A. J. P. Teunissen, Z. A. Fayad, C. Calcagno, G. J. Strijkers and W. J. M. Mulder, *Nat. Nanotechnol.*, 2020, **15**, 398–405.

141 S. Lim, H. Y. Yoon, H. J. Jang, S. Song, W. Kim, J. Park, K. E. Lee, S. Jeon, S. Lee, D. K. Lim, B. S. Kim, D. E. Kim and K. Kim, *ACS Nano*, 2019, **13**, 10991–11007.

142 Y. Zhang, H. Zhang, B. Li, H. Zhang, B. Tan and Z. Deng, *Nano Res.*, 2018, **11**, 1625–1641.

143 J. Liu, J. Xu, J. Zhou, Y. Zhang, D. Guo and Z. Wang, *Int. J. Nanomed.*, 2017, **12**, 1113–1126.

144 C. Verry, S. Dufort, B. Lemasson, S. Grand, J. Pietras, I. Troprès, Y. Crémillieux, F. Lux, S. Mériaux, B. Larrat, J. Balosso, G. L. Duc, E. L. Barbier and O. Tillement, *Sci. Adv.*, 2020, **6**, eaay5279.

145 H. Lin, X. Tang, A. Li and J. Gao, *Adv. Mater.*, 2021, **33**, 2005657.

146 X. Tang, X. Gong, A. Li, H. Lin, C. Peng, X. Zhang, X. Chen and J. Gao, *Nano Lett.*, 2020, **20**, 363–371.

147 X. Zhu, X. Tang, H. Lin, S. Shi, H. Xiong, Q. Zhou, A. Li, Q. Wang, X. Chen and J. Gao, *Chem*, 2020, **6**, 1134–1148.

148 X. Tang, X. Gong, J. Ming, D. Chen, H. Lin and J. Gao, *Anal. Chem.*, 2020, **92**, 16293–16300.
149 Z. Ding, H. Sun, S. Ge, Y. Cai, Y. Yuan, Z. Hai, T. Tao, J. Hu, B. Hu, J. Wang and G. Liang, *Adv. Funct. Mater.*, 2019, **29**, 1903860.
150 H. Li, D. Luo, C. Yuan, X. Wang, J. Wang, J. P. Basilion and T. J. Meade, *J. Am. Chem. Soc.*, 2021, **143**, 17097–17108.
151 R. Yan, Y. Hu, F. Liu, S. Wei, D. Fang, A. J. Shuhendler, H. Liu, H. Y. Chen and D. Ye, *J. Am. Chem. Soc.*, 2019, **141**, 10331–10341.
152 Y. Hu, J. Zhang, Y. Miao, X. Wen, J. Wang, Y. Sun, Y. Chen, J. Lin, L. Qiu, K. Guo, H. Y. Chen and D. Ye, *Angew. Chem., Int. Ed.*, 2021, **60**, 18082–18093.
153 C. A. Cheng, W. Chen, L. Zhang, H. H. Wu and J. I. Zink, *J. Am. Chem. Soc.*, 2019, **141**, 17670–17684.
154 H. Zhao, J. Lv, F. Li, Z. Zhang, C. Zhang, Z. Gu and D. Yang, *Biomaterials*, 2021, **268**, 120591.
155 T. T. Zhang, C. H. Xu, W. Zhao, Y. Gu, X. L. Li, J. J. Xu and H. Y. Chen, *Chem. Sci.*, 2018, **9**, 6749–6757.
156 F. Xu, J. Zhu, L. Lin, C. Zhang, W. Sun, Y. Fan, F. Yin, J. C. M. van Hest, H. Wang, L. Du and X. Shi, *Theranostics*, 2020, **10**, 4349–4358.
157 C. Liu, D. Wang, S. Zhang, Y. Cheng, F. Yang, Y. Xing, T. Xu, H. Dong and X. Zhang, *ACS Nano*, 2019, **13**, 4267–4277.
158 D. Liu, Z. Zhou, X. Wang, H. Deng, L. Sun, H. Lin, F. Kang, Y. Zhang, Z. Wang, W. Yang, L. Rao, K. Yang, G. Yu, J. Du, Z. Shen and X. Chen, *Biomaterials*, 2020, **244**, 119979.
159 K. Deng, B. Wu, C. X. Wang, Q. Wang, H. Yu, J. M. Li, K. H. Li, H. Y. Zhao and S. W. Huang, *Adv. Healthcare Mater.*, 2020, **9**, 2000533.